

**Testing the Production of Scintillation Arcs with  
the Pulsar B1133+16**

**Stella Koch Ocker**

A thesis presented in partial fulfillment of the requirements  
for the degree of Bachelor of Arts

Department of Physics and Astronomy  
Oberlin College  
Oberlin, OH  
March 2018

# Summary

A pulsar is an extremely dense, highly magnetized star with a radio wave lighthouse beam that sweeps across the sky. It produces highly regular pulses if the beam sweeps past the Earth, and the pulse period can be as short as a few milliseconds. The arrival times of pulsar radio signals at Earth observatories can be used as a clock precise enough to detect gravitational waves. Performing such a detection requires the mitigation of interference effects from the interstellar medium: the slightly ionized, mostly hydrogen gas that the radio waves traverse as they travel from the pulsar to Earth. We investigate radio wave delays using a powerful tool: scintillation arcs, fluctuations in frequency and time of the pulsar signal intensity that are manifested as parabolic arcs in the pulsar's secondary spectrum. While scintillation arcs were first observed by Oberlin students almost two decades ago, the structures that cause them are still unknown. Observational and theoretical efforts over the past 17 years suggest that the arcs might arise from thin, highly elongated plasma formations that are effectively one-dimensional perpendicular to the line of sight to the pulsar.

We explore the unique capabilities of the pulsar B1133+16 for testing models of scintillation arcs. Using measurements of scintillation arc curvatures over 96 days, we test a model for the annual modulation of arc curvature due to Earth's orbit. The formalism for determining the width of a pulsar image from a scintillation arc width is used to design an empirical test of scintillation arc models based on the frequency dependence of arc widths. This formalism is then explored in the framework of a simple, one-dimensional model for the production of scintillation arcs.

# Dedication

To my parents, for your constant support and guidance.

# Acknowledgements

Much of this thesis consists of a fruitful collaboration between my Honors advisor Dan Stinebring, Barney Rickett (Professor Emeritus at UC San Diego), and myself. Dan has been an invaluable mentor throughout my Oberlin education. His constant support and faith in my abilities have fueled my passion for astrophysics, and his mentorship and guidance have been crucial to the completion of this project. Thanks to Dan and NANOGrav, I have had the opportunity to travel the world and participate in the international pulsar community, cementing my desire to continue in the field. Barney Rickett has also been a generous source of insight throughout this project, and his modeling work inspired significant portions of this thesis. Thank you Barney for your wise suggestions. Thanks are also due to Stefan Osłowski, Joris Verbiest, and Lars Küinkel, who generously provided data for this project.

# Contents

<b>1 Pulsars and the Interstellar Medium</b>	<b>12</b>
1.1 The Known Pulsar Population . . . . .	12
1.2 Gravitational Waves and Pulsar Timing . . . . .	15
1.3 Sources of Noise: the Interstellar Medium . . . . .	18
<b>2 Introduction to Scintillation Arcs</b>	<b>23</b>
2.1 Observational Basics . . . . .	23
2.2 Theory . . . . .	24
2.2.1 Scattering off a Thin Screen . . . . .	24
2.2.2 Dynamic and Secondary Spectra . . . . .	27
2.2.3 Proposed Models . . . . .	27
2.3 Key Observational Results . . . . .	29
2.4 Purpose of the Thesis . . . . .	30
<b>3 Annual Arc Curvature Modulation</b>	<b>32</b>
3.1 Theory . . . . .	32
3.2 Observational Data and Methods . . . . .	35
3.3 Results . . . . .	39
3.4 Discussion . . . . .	42
<b>4 The Frequency Dependence of Scintillation Arc Widths</b>	<b>45</b>
4.1 Determining the Width of a Scattered Pulsar Image . . . . .	45
4.2 Frequency Dependence of B1133+16 Arc Widths . . . . .	48
4.2.1 Observational Data and Methods . . . . .	48
4.2.2 Results . . . . .	49

4.3 Discussion . . . . .	53
<b>5 Exploring Models with Arc Width Analysis</b>	<b>56</b>
5.1 A Collection of Simple Models . . . . .	56
5.2 A 1D Scattered Image Model . . . . .	58
5.3 A 1D Gaussian/Power-Law Model . . . . .	63
5.3.1 A 1D Mechanism for Broadening Arcs . . . . .	63
5.4 A 1D Model of B1133+16 . . . . .	68
5.5 Discussion . . . . .	68
<b>6 Conclusions</b>	<b>70</b>
<b>A Derivation of Annual Curvature Modulation</b>	<b>73</b>
<b>References</b>	<b>79</b>

# List of Figures

1.1	A sample of pulse profiles for different pulsars (Lorimer 2008).	14
1.2	An example of a $P-\dot{P}$ diagram (Lorimer 2008). Dashed lines correspond to constant magnetic field, dashed-dotted correspond to constant characteristic age, and dotted correspond to constant spin-down energy loss. Normal pulsars lie in the upper-middle half of the plot, and millisecond pulsars lie in the lower left. . . . .	15
1.3	The spectrum of gravitational wave strains detectable through the cosmic microwave background, Pulsar Timing Arrays, space-based interferometers like eLISA, and ground-based interferometers like LIGO. Figure courtesy of NANOGrav.org. . . . .	17
1.4	An example of dispersion (Lorimer 2008). The top part of the plot shows the dispersed arrival of different frequency components of the pulse as a function of pulse phase (or periods of rotation). The pulse profile is shown at the bottom. Lower frequency components of the pulse take longer to arrive than higher frequency components. . . . .	20
1.5	A schematic demonstrating pulse broadening (Lorimer 2008).	22
1.6	An example of diffractive scintillation in a dynamic spectrum of the pulsar B1133+16. Diffractive scintillation is characterized by fluctuations in frequency and time of the pulsar emission intensity, on timescales of minutes to hours (Armstrong et al. 1995). Figure courtesy of Dan Stinebring. . . . .	22

2.1	Dynamic and secondary spectra from three observations of PSR B1133+16, displaying a variety of scintillation behavior (Cordes et al. 2006). . . . .	25
2.2	A basic diagram of the thin screen scattering geometry, indicating the screen location $s$ and the scattering angles corresponding to waves scattered in directions $\theta_1$ and $\theta_2$ . . . . .	26
2.3	The scattered image of the pulsar B0834+06 (Brisken et al. 2010), determined using VLBI and the secondary spectrum of the pulsar. Lower and higher precision astrometric measurements are shown in cyan and red, respectively. . . . .	29
3.1	Expected curvature modulation for B1133+16 over a year long cycle beginning on MJD (Modified Julian Day number) 57083, assuming the scattering image is aligned with $\mathbf{v}_{\text{eff}}$ and the screen is effectively stationary ( $\mathbf{v}_{\text{scr}\perp} \approx 0$ ). The observing frequency was taken to be 1450 MHz. . . . .	34
3.2	Dynamic and secondary spectra for B1133+16, displaying three distinct scintillation arcs. The spectra were taken on 2015 March 2 at Arecibo Observatory at 1450 MHz. Figure courtesy of Dan Stinebring. . . . .	36
3.3	Dynamic and secondary spectra for B1133+16, displaying a single distinct scintillation arc. The spectra were taken on 2015 June 6 at Arecibo Observatory at 1450 MHz. Figure courtesy of Dan Stinebring. . . . .	37
3.4	Average intensity vs. curvature plot produced by running $\mathbf{v}_{\text{eff}}$ on a secondary spectrum of B1133+16. The three peaks correspond to the curvatures that matched the largest number of pixel bins (represented here in mean dB, the bin intensity). . . . .	38
3.5	Measured curvatures for three distinct scintillation arcs detected in secondary spectra for B1133+16 over a 96 day span of observations at 1450 MHz. Curvatures for the outer, middle, and inner arcs are shown in blue, orange, and green, respectively. . . . .	38

3.6	Measured curvatures and the corresponding curvatures for best values of $s$ determined with a nonlinear least squares fit. The fit was calculated using the annual modulation model described in Section 3.1, under the assumption that the $\mathbf{v}_{\text{scr}} \approx 0$ and $\psi = 0^\circ$ . . . . .	39
3.7	Measured and fitted curvatures, as in Fig. 3.6, for $\psi = 20^\circ$ . . . . .	40
3.8	Measured and fitted curvatures, as in Fig. 3.6, for $\psi = 40^\circ$ . . . . .	41
3.9	Measured and fitted curvatures, as in Fig. 3.6, for $\psi = 60^\circ$ . . . . .	41
3.10	Measured and fitted curvatures, as in Fig. 3.6, for $\psi = 80^\circ$ . . . . .	42
3.11	Secondary spectrum for B1133+16 at 327 MHz, taken on MJD 57058. At least two scintillation arcs are visible. . . . .	44
3.12	Average pixel intensity vs. curvature for the secondary spectrum taken on MJD 57058 at 327 MHz, shown above. . . . .	44
4.1	Geometry of a linear, highly elongated pulsar image tilted at an angle $\psi$ with respect to $\mathbf{v}_{\text{eff}}$ , which is aligned with the $\theta_x$ axis. The pulsar is depicted in blue and the scattered image in gray (not to scale). The relevant widths $\Delta\theta_x$ and $w$ are also shown. In this geometry, $w$ does not depend on observing frequency. . . . .	47
4.2	A cross-cut of the linear pixel intensity averaged over 20 delay rows, taken from the secondary spectrum of B1133+16 on MJD 57090 at 327 MHz. The fitted Gaussian functions are shown in red. . . . .	48
4.3	Measured arc widths in $f_t$ vs. delay in $\mu\text{s}$ at 125 MHz. The widths of the negative $f_t$ arc are shown in green. The scintillation arc was one-sided in the negative $f_t$ quadrant of the secondary spectrum. . . . .	50
4.4	Measured arc widths vs. delay at 327 MHz. The widths of the negative $f_t$ arc are shown in green, and the widths of the positive $f_t$ arc are shown in blue. . . . .	51
4.5	Measured arc widths vs. delay at 432 MHz. The arc widths are labeled as in Fig. 4.4. . . . .	51

4.6	Measured arc widths vs. delay for the middle arc at 1450 MHz. The arc widths are labeled as in Fig. 4.4. . . . . .	52
4.7	Average width in $f_t$ as a function of observing frequency. The y-axis is $\log(f_t)$ , while the x-axis shows $\log(\nu)$ . The average widths are shown in blue. A weighted linear least squares fit on the widths is shown in red, corresponding to a slope of $-0.8 \pm 0.1$ . . . . .	52
4.8	The secondary spectrum of B1133+16 on MJD 57094 at 125 MHz. The curvature measured at 327 MHz on MJD 57090, re-scaled to 125 MHz, is shown in blue. Figure courtesy of Lars Künkel. . . . .	55
4.9	The linear intensity cross-cut of the secondary spectrum shown in Fig. 4.8 at a delay of $30.0 \mu\text{s}$ . . . . .	55
5.1	Six basic scattered image models. Models (a) and (b) are a highly elongated, 1D pulsar image with a bright, point-like core and a bright, broadened core, respectively. Models (c) and (d) are a broad, elongated image with a bright, broad core and a bright, point-like core, respectively. Model (e) is an elongated, 1D pulsar image with 1D bright “patches,” and model (f) is a bright, point-like core with a broad, scattered halo. . . . .	57
5.2	Behavior of the angles $\theta_+$ (in black) and $\theta_-$ (in red) as a function of dimensionless fringe frequency $q$ for crosscuts of the secondary spectrum at dimensionless delays $p = 5, 10, 15, 20$ (thin to thick lines). The secondary spectrum is assumed to arise from a 1D scattered image of the form given in Eq. 5.1. The circled points indicate the value of $\theta_-$ when the corresponding $\theta_+ = 0$ as the crosscut passes across the center of the scintillation arc. . . . .	60

5.3 The brightness function for a scattered image consisting of a Gaussian core with an amplitude  $B_0 = 1$  and a width  $\theta_1 = 1$ , which crosses over at a power level of -10 dB to a power-law with an index of 2. . . . . 62

5.4 Secondary spectrum extracted from a 1D scattered image consisting of a Gaussian core with  $B_0 = 1$  and  $\theta_s = 0.1$ , which crosses over at a power level of -20 dB to a power-law with an index of 2. Here the angle between the scattered image and the effective velocity is  $\psi = 0^\circ$ . . . . . 64

5.5 Secondary spectrum extracted from the 1D Gaussian/power-law image of the same parameters as in Fig. 5.4, but here  $\psi = 20^\circ$ . . . . . 64

5.6 Secondary spectrum extracted from the 1D Gaussian/power-law image of the same parameters as in Fig. 5.4, but here  $\psi = 40^\circ$ . . . . . 65

5.7 Secondary spectrum extracted from the 1D Gaussian/power-law image of the same parameters as in Fig. 5.4, but here  $\psi = 60^\circ$ . . . . . 65

5.8 Cross-cuts of the linear intensity as a function of  $q$  at  $p = 5, 10, 15,$  and  $20$ . The scattered image was taken to have a Gaussian core width of  $0.1$ , angled at  $\psi = 0^\circ$  with respect to the effective velocity. . . . . 66

5.9 Cross-cuts of the linear intensity as a function of  $q$  at  $p = 5, 10, 15,$  and  $20$ . The scattered image was taken to have a Gaussian core width of  $0.2$ , angled at  $\psi = 0^\circ$  with respect to the effective velocity. . . . . 66

5.10 Cross-cuts of the linear intensity as a function of  $q$  at  $p = 5, 10, 15,$  and  $20$ . The scattered image was taken to have a Gaussian core width of  $0.4$ , angled at  $\psi = 0^\circ$  with respect to the effective velocity. . . . . 67

5.11	Cross-cuts of the linear intensity as a function of $q$ at $p = 5$ , 10, 15, and 20. The scattered image was taken to have a Gaussian core width of 0.6, angled at $\psi = 0^\circ$ with respect to the effective velocity. . . . .	67
5.12	Cross-cuts of secondary spectra at $p = 10$ for values of $\psi$ ranging from $0^\circ$ to $80^\circ$ . All other parameters of the scattered image were kept the same. . . . .	68

# Chapter 1

## Pulsars and the Interstellar Medium

Pulsars are some of the most compact objects in our Universe. With diameters on the order of kilometers and masses on the order of  $10^{30}$  kg, these stars host vast amounts of rotational energy manifesting itself in rotational periods as short as milliseconds and magnetic fields as large as  $10^{15}$  G (Kalapotharakos et al. 2012). Their rotational stability makes pulsars extremely precise clocks, invaluable tools for studying the physics of gravity, relativity, the interstellar medium, and more.

### 1.1 The Known Pulsar Population

Pulsars are part of a large population of compact, astrophysical objects called neutron stars. Formed from supernovae, neutron stars have a rigid, crystalline outer crust of neutron-rich nuclei. As pressure increases towards the stellar interior, these nuclei become more neutron rich until they are surrounded by a degenerate neutron superfluid (D'Alessandro 1996). While the exact substance of the neutron star core remains unknown, much has been learned from the electromagnetic emission of pulsars, which are the most-studied neutron stars to date (Kaspi & Kramer 2016).

Of an estimated 70,000 observable pulsars in our Galaxy, about 2,300

are known (Lyne et al. 1985; Kaspi & Kramer 2016). With lifetimes on the order of  $10^6$  years (Lyne et al. 1985), these stars are born traveling at a mean velocity of about 400 km/s (Hobbs et al. 2005). Pulsars emit electromagnetic radiation from magnetic poles offset from their rotation axes, and are so named for the pulses of radiation that pass in and out of an observer's line of sight as the pulsar rotates. While the physical cause of this emission is still unknown, it has been widely observed in the radio band, in addition to the X-ray and  $\gamma$ -ray bands (Kaspi & Kramer 2016). Observing in these different emission bands provides various kinds of information about a pulsar. For example, X-ray observations are useful for their spectral cyclotron lines, which can be used as a direct measure of magnetic field (Caballero & Wilms 2012), while  $\gamma$ -ray observations are useful probes of particle acceleration in the magnetosphere (Grenier & Harding 2015). Radio observations, which will be used in this thesis, are the primary source for studies on gravitational wave physics and the interstellar medium (ISM).

A pulse of radio emission from a pulsar is characterized by a pulse profile. While individual pulses are difficult to detect, and differ in the shape of their intensity, stacking thousands of radio observations of a single pulsar will result in a high signal-to-noise, average pulse profile that remains very stable over time (Lommen & Demorest 2013). Examples of different pulse profiles are shown in Fig. 1.1. Variations in pulse profile morphology are likely due to a pulsar's age, the emission mechanism, and the presence of a binary companion (Lorimer 2008). These profiles are a key ingredient in pulsar timing. Using the average pulse profile, a model can be created for a pulse time of arrival (TOA). With more data, more TOAs can be calculated and the model improved, until highly precise predictions of TOAs can be made (Lommen & Demorest 2013). Slight deviations from the predicted TOA of a pulsar can then be used to measure key characteristics, including proper motion, orbital parameters, spin period ( $P$ ), and spin-down rate ( $\dot{P}$ ) (Hobbs et al. 2005).

Pulsars spin down due to rotational kinetic energy loss through both electromagnetic emission and the ejection of a relativistic, highly magnetized electron-positron plasma, the pulsar wind (Lyne 1999; Kargaltsev et al.

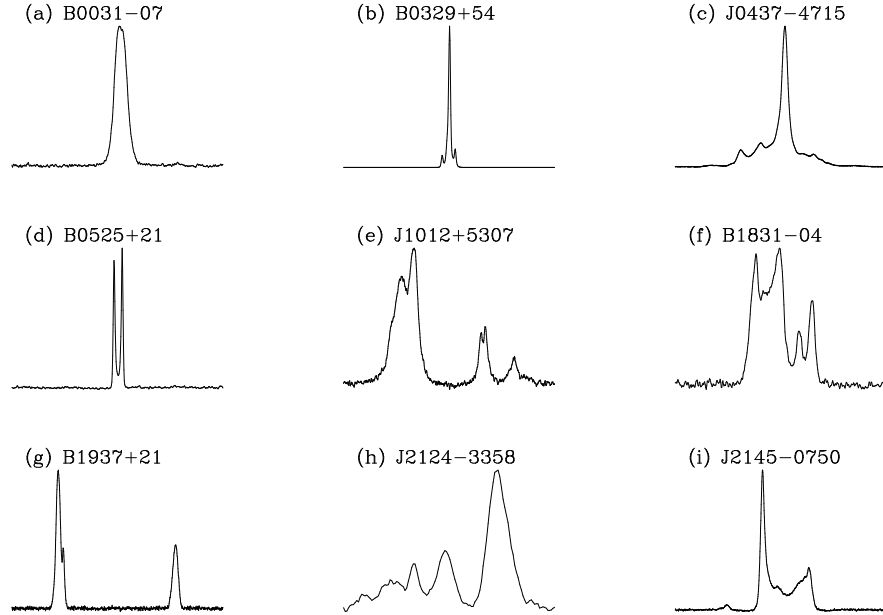


Figure 1.1: A sample of pulse profiles for different pulsars (Lorimer 2008).

2015; Usov 2003). The known pulsar population remains significantly limited by observational selection biases in pulsar surveys and the scattering of pulsar signals in the ISM (Kaspi & Kramer 2016). However, comparing spin and spin down rates in a so-called  $P-\dot{P}$  diagram serves as a useful diagnostic of the currently known population. An example of a  $P-\dot{P}$  diagram is given in Fig. 1.2. Not only are  $P$  and  $\dot{P}$  used to estimate a pulsar's characteristic (or upper limit) age, magnetic field strength, and spin-down luminosity (Kaspi & Kramer 2016), but their distribution for different pulsars in the  $P-\dot{P}$  diagram also reveals two different groups within the pulsar population: normal pulsars and millisecond pulsars (MSPs).

MSPs lie in the low  $P$ , low  $\dot{P}$  section of the  $P-\dot{P}$  diagram, and are named for their millisecond-scale periods (the fastest has a period of 1.56 ms (Kramer 2004)). Their unusually fast rotation rate is due to spin-up driven by the accretion of a binary companion star (Kaspi & Kramer 2016).

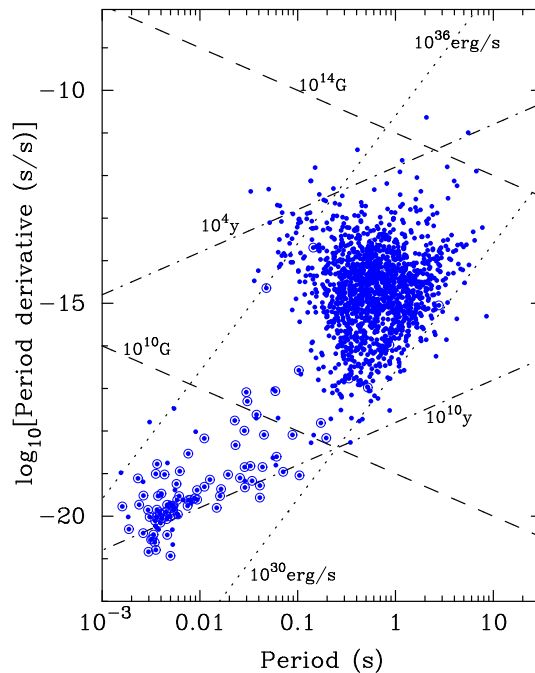


Figure 1.2: An example of a  $P$ - $\dot{P}$  diagram (Lorimer 2008). Dashed lines correspond to constant magnetic field, dashed-dotted correspond to constant characteristic age, and dotted correspond to constant spin-down energy loss. Normal pulsars lie in the upper-middle half of the plot, and millisecond pulsars lie in the lower left.

Their short periods also make them ideal sources for pulsar timing, since MSP TOAs can be measured to even higher precision than for normal pulsars. Such high-precision timing can be used for a number of applications, most notably the detection of gravitational waves.

## 1.2 Gravitational Waves and Pulsar Timing

Pulsars have already been successfully used to indirectly detect gravitational waves (GWs). In 1974, Russell Hulse and Joe Taylor discovered the first bi-

nary pulsar system, which showed the effects of gravitational redshift and relativistic spin precession, thus indirectly confirming the relativistic prediction of GWs (Kaspi & Kramer 2016). Binary pulsars are still being used to test General Relativity, including the famous double pulsar, discovered in 2003 and used to perform one of the highest-precision tests of GR in a strong field to date (Kramer & Stairs 2008). While the existence of GWs has already been directly confirmed by LIGO, pulsar timing can be used to directly measure lower frequency GWs than those measurable with LIGO and other GW detectors.

Suppose a GW travels through spacetime and encounters a pulsar signal propagating towards Earth. That GW will cause a delay in the pulsar signal's arrival time at an Earth telescope. There will be a discrepancy between the pulse's expected TOA, calculated from a timing model, and its measured TOA. Taking all other causes of pulse TOA delays into account, the residual between the expected and measured TOAs should bear the signature of a GW (Burke-Spolaor 2015). In reality, such a GW detection would be made using a Pulsar Timing Array (PTA), an array of MSPs that are timed to high precision and which can be used as a galactic-scale interferometer capable of localizing the GW source.

There are three major PTAs currently hunting for GWs: the North American Nanohertz Observatory for Gravitational Waves (NANOGrav), the European Pulsar Timing Array (EPTA), and the Parkes Pulsar Timing Array (PPTA), which together form an international consortium known as the International Pulsar Timing Array (IPTA). The sensitivities of different GW detectors are shown in Fig. 1.3. Unlike other GW detectors, PTAs are sensitive to GWs with nHz to  $\mu$ Hz frequencies (Burke-Spolaor 2015). This sensitivity range will probe a variety of GW phenomena, including GWs produced by cosmic strings and binary supermassive black hole (BSMBH) mergers (Burke-Spolaor 2015). PTAs are thus capable of providing unique information about certain GW sources, like the BSMBHs that are predicted to exist in large quantities through galaxy mergers (Sesana 2013).

Performing such a detection with PTAs requires the mitigation of noise from a variety of sources. Pulsars exhibit two main, intrinsic irregularities

### The spectrum of gravitational wave astronomy

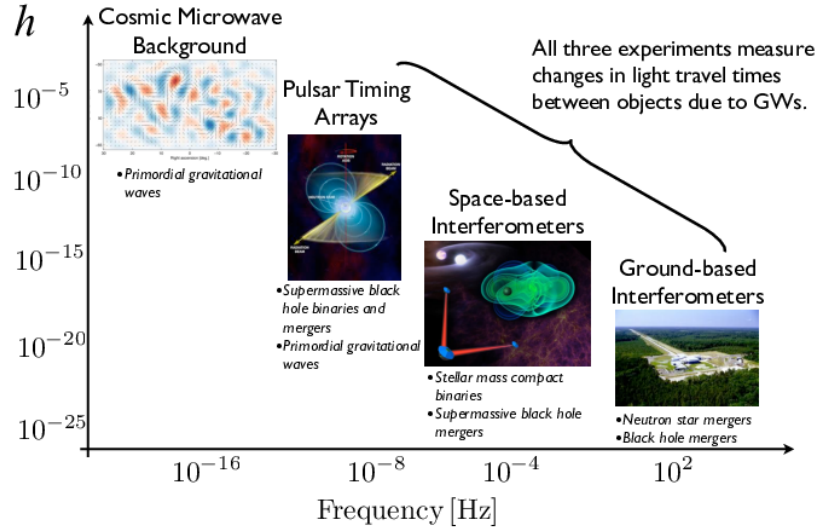


Figure 1.3: The spectrum of gravitational wave strains detectable through the cosmic microwave background, Pulsar Timing Arrays, space-based interferometers like eLISA, and ground-based interferometers like LIGO. Figure courtesy of NANOGrav.org.

in  $P$  and  $\dot{P}$ . Timing noise is a long, continuous, unpredictable fluctuation in measured TOAs relative to normal spin down, while glitches are short, discontinuous, unpredictable increases in  $P$  followed by an exponential relaxation back to the original  $\dot{P}$  (D'Alessandro 1996). The subject of this thesis is yet another major source of noise in pulsar timing, scattering in the ISM.

### 1.3 Sources of Noise: the Interstellar Medium

The ISM is comprised of a vast range of materials and objects, from clouds of molecular gas and plasma to meteorites. With an average electron density of just  $0.1 \text{ cm}^{-3}$  (Gurnett et al. 2013), the ISM also contains a variety of molecular abundances, usually found in the form of gas or dust (Herbst & van Dishoeck 2009). The most abundant molecule,  $\text{H}_2$ , forms on dust grains primarily produced by stars and supernovae (Savage & Mathis 1979; Popping et al. 2017), while molecules with six or more atoms (“complex,” by astrophysical standards) are typically found in denser gas or dust clouds (Herbst & van Dishoeck 2009).

Ranging widely in density and temperature, these clouds contain valuable information about star formation and nucleosynthesis (Wilson & Rood 1994). Dust is believed to catalyze molecular formation in the ISM; it also acts as a cooling channel for gas by absorbing ultraviolet stellar radiation and re-emitting it in the infrared (Popping et al. 2017). The internal structure and dynamics of molecular clouds are often studied with spectroscopy: the identification of molecular absorption and emission lines in a spectral observation reveals both the content of and distance to a molecular cloud (Wilson & Rood 1994).

In spite of thorough studies on molecular abundances and cloud formations in the ISM, much remains unknown about both large and small-scale interstellar structures. One of the dominant theories for large-scale structure relies on regulation by supernovae. According to the McKee & Ostriker model, ISM structure can be divided into concentric clouds of a cold neutral medium (CNM), warm neutral medium (WNM), warm ionized medium (WIM), and hot ionized medium (HIM), all in rough pressure balance with each other. By creating large volumes of hot, low-density gas, supernovae regulate and drive the formation of this large-scale structure (McKee & Ostriker 1977). Due to the relatively frequent occurrence of supernovae, such a model remains attractive today (Breitschwerdt et al. 2012), and CNM, WNM, WIM, and HIM remain useful designations for different interstellar environments (Haverkorn & Spangler 2013).

Studies probing interstellar structure often take advantage of propagation effects in the ISM. As light travels from stars to Earth, it encounters different structures which scatter, absorb, delay, or otherwise interfere with that light. The sum of absorption and scattering effects on an observed signal is called extinction, and results in the dimming and reddening of a source (Savage & Mathis 1979; Marshall et al. 2006). Made using spectral and photometric data, extinction maps are one method of mapping the distribution of material in the ISM, and can be used to mitigate extinction effects in other observations (Marshall et al. 2006).

Due to their high spatial coherence (i.e., they behave like point sources), pulsars are particularly sensitive to a variety of propagation effects in the ISM (Cordes & Lazio 2002):

- **Dispersion** refers to a time delay between the arrival of lower frequency and higher frequency components of a pulse signal at a telescope. Lower frequency components are more sensitive to electron density variations along the line of sight, and thus take longer to arrive at a telescope than higher frequency components. An example of dispersion is shown in Fig. 1.4. The time delay between high and low frequency pulses depends on the electron density along the line of sight, which is quantified using dispersion measure (DM):

$$DM = \int_0^d n_e dl \quad (1.1)$$

where  $d$  is the distance to the pulsar and  $n_e$  is the electron density (Lorimer 2008). By comparing DM measurements with a model for the distribution of galactic free electrons (e.g., see (Cordes & Lazio 2002) or (Yao et al. 2017)), DM can be used to measure the distances to pulsars.

- **Scattering** refers to a range of propagation effects driven by the scattering of pulse signals off of intervening material in the ISM.
  - *Pulse broadening* is a lengthening of the tail of a detected pulse. A schematic demonstrating this effect is shown in Fig. 1.5 (Lorimer 2008).

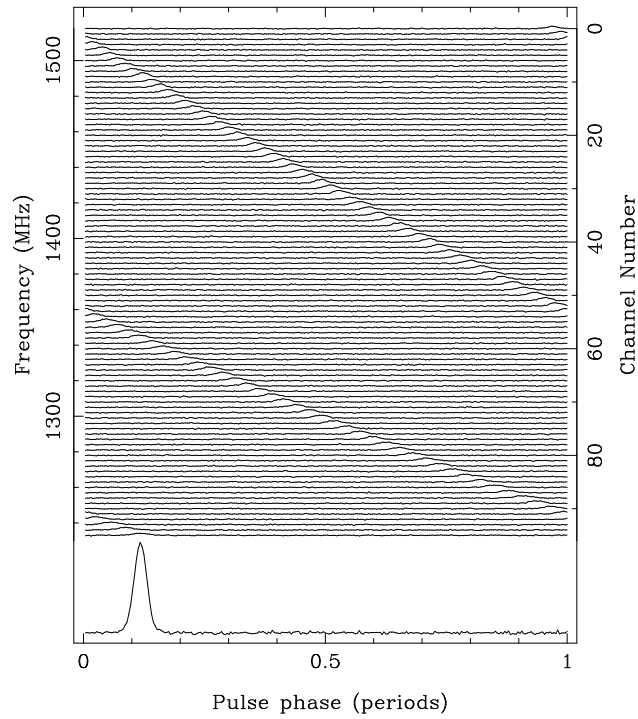


Figure 1.4: An example of dispersion (Lorimer 2008). The top part of the plot shows the dispersed arrival of different frequency components of the pulse as a function of pulse phase (or periods of rotation). The pulse profile is shown at the bottom. Lower frequency components of the pulse take longer to arrive than higher frequency components.

- *Angular broadening* is a smearing out of the pulsar image. The pulsar appears blurred-out instead of point-like.
- *Interstellar scintillation (ISS)* is fluctuation in pulsar emission intensity due to interference between scattered beams of a pulse signal (Rudnitskii et al. 2017). Diffractive ISS occurs on timescales of minutes to hours, while refractive ISS occurs in days to months (Armstrong et al. 1995). An example of diffractive ISS is given in Fig. 1.6. ISS tends to increase with pulsar distance and observing wavelength (Rickett 1990), and is likely caused by plasma irregularities in the ISM (Armstrong et al. 1995). Since ISS also changes depending on the relative motion of pulsars, the ISM, and Earth, it is used to determine astrometric parameters like pulsar velocity (Kramer & Stairs 2008). More introduction to ISS is given in Chapter 2.

The propagation effects described above bear significant consequences for the detection of GWs with pulsar timing. If PTAs hope to detect GWs with nHz to  $\mu$ Hz frequencies, all dispersive and scattering effects must be properly mitigated. However, certain effects like ISS are not fully understood. The origins of ISS and its behavior with time and observing frequency remain crucial, open questions.

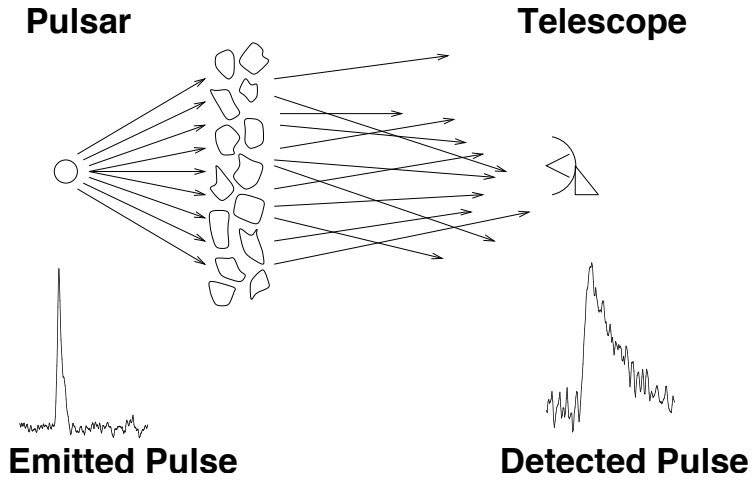


Figure 1.5: A schematic demonstrating pulse broadening (Lorimer 2008).

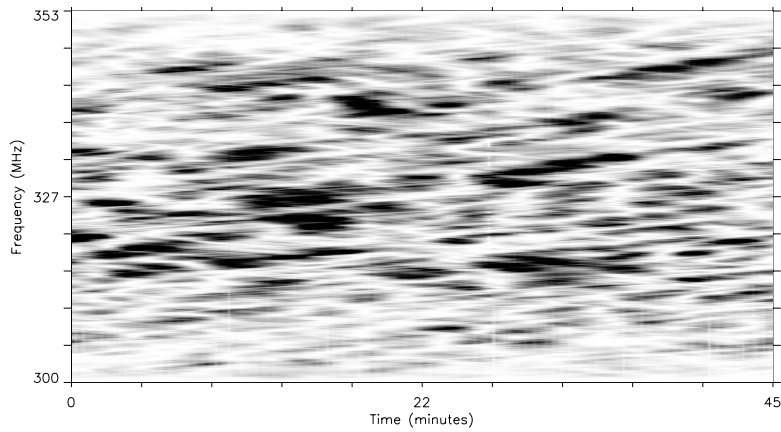


Figure 1.6: An example of diffractive scintillation in a dynamic spectrum of the pulsar B1133+16. Diffractive scintillation is characterized by fluctuations in frequency and time of the pulsar emission intensity, on timescales of minutes to hours (Armstrong et al. 1995). Figure courtesy of Dan Stinebring.

## Chapter 2

# Introduction to Scintillation Arcs

Interstellar scintillation (ISS) can be used to probe a variety of structures in the interstellar medium (ISM). As discussed in Chapter 1, diffractive ISS (DISS) is characterized by fluctuations in the flux density of pulsar emission in radio frequency and time (Stinebring 2007). Flux density as a function of frequency and time composes a dynamic spectrum, an example of which is shown in Fig. 1.6. In the dynamic spectrum, DISS is evident as “scintles,” or elongated patches of power that drift across the spectrum through time. In 2001, Stinebring et al. (2001) performed a 2D Fourier transform on the dynamic spectra of 30 pulsars, and in the so-called “secondary spectra” of 4 pulsars found faint parabolic arcs. These scintillation arcs imply the existence of small, highly elongated plasma formations in the ISM, the astrophysical nature of which is still unknown.

### 2.1 Observational Basics

Scintillation arcs have been observed in over 20 pulsars and over frequencies ranging from 125 MHz to 1450 MHz and higher (Stinebring 2007; Hill et al. 2003). While scintillation arcs appear to be an almost ubiquitous phenomenon, they range widely in behavior, from thin, uniformly distributed

parabolas to patchy inverted “arclets,” as shown in Fig. 2.1.

The key observational features of scintillation arcs are the following:

- The **curvature** of a scintillation arc is obtained by fitting a simple parabola to the arc by eye or using an automated method. The temporal behavior of scintillation arc curvature can yield valuable information about the motion of the pulsar with respect to Earth, and the source of scattering (see Chapter 3).
- Since the **power distribution** of a secondary spectrum is related to the distribution of scattering material on the sky and the pulsar’s motion through space, we are developing tools to explore it quantitatively. Measuring the **arc width** is one method of characterizing this power distribution (see Chapter 4).
- The **frequency dependence** of scintillation arc curvatures and widths is a valuable test of different models for the production of scintillation arcs (see Chapter 5).

## 2.2 Theory

### 2.2.1 Scattering off a Thin Screen

The secondary spectrum,  $S_2(f_\nu, f_t)$  is defined to be the 2D power spectrum of the dynamic spectrum,  $S(\nu, t)$ , which is flux density as a function of radio frequency  $\nu$  and time  $t$  (Hill et al. 2003):

$$S_2(f_\nu, f_t) = |\tilde{S}(\nu, t)|^2 \quad (2.1)$$

where  $f_\nu$  and  $f_t$  denote conjugate  $\nu$  and conjugate  $t$ , and from here on will be referred to as delay and fringe frequency, respectively.

The basic scintillation arc phenomenon can be explained by scattering off of a thin screen of ionized gas. When radiation from a point source (or pulsar) encounters the screen and then travels to the observer through deflected paths, the scattered waves will interfere to produce scintillation

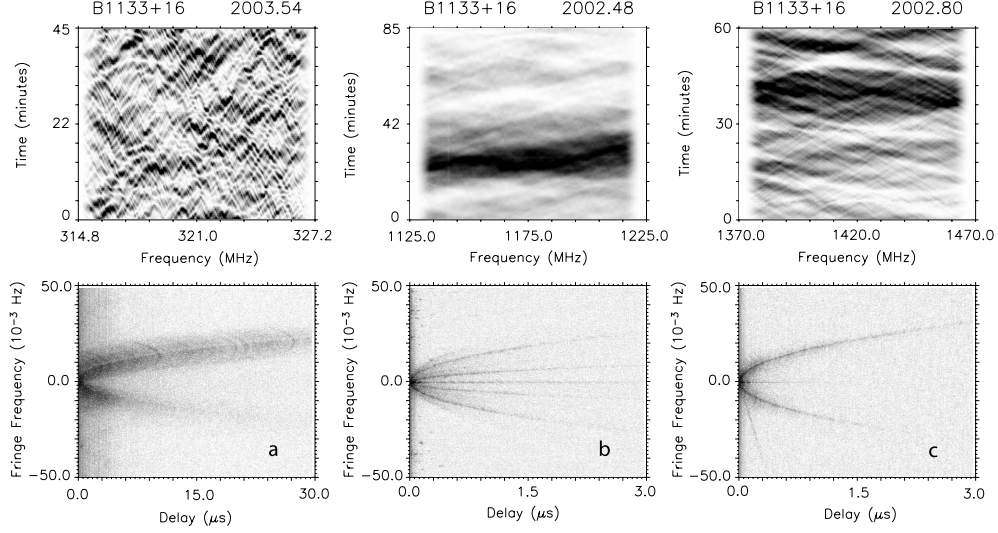


Figure 2.1: Dynamic and secondary spectra from three observations of PSR B1133+16, displaying a variety of scintillation behavior (Cordes et al. 2006).

(Cordes et al. 2006). A diagram of the scattering geometry is shown in Fig. 2.2. For two waves arriving at the observer from directions  $\theta_1$  and  $\theta_2$ ,

$$f_\nu = \frac{D(1-s)}{2cs}(\theta_2^2 - \theta_1^2) \quad (2.2)$$

$$f_t = \frac{1}{\lambda s}(\theta_2 - \theta_1) \cdot \mathbf{v}_{\text{eff}} \quad (2.3)$$

where  $D$ ,  $c$ , and  $\lambda$  are the distance to the pulsar, the speed of light, and the observing wavelength, respectively (Cordes et al. 2006). The screen location is given by  $s$ , a dimensionless factor of the distance between the observer and the pulsar,

$$s = \frac{D_{\text{psr-screen}}}{D_{\text{tot}}}, 0 \leq s \leq 1. \quad (2.4)$$

Finally,  $\mathbf{v}_{\text{eff}}$  refers to the effective screen velocity, i.e., the velocity of a point in the screen intersected by a straight line from observer to pulsar:

$$\mathbf{v}_{\text{eff}} = (1-s)\mathbf{v}_{\text{p}\perp} + s\mathbf{v}_{\text{obs}\perp} - \mathbf{v}_{\text{scr}\perp} \quad (2.5)$$

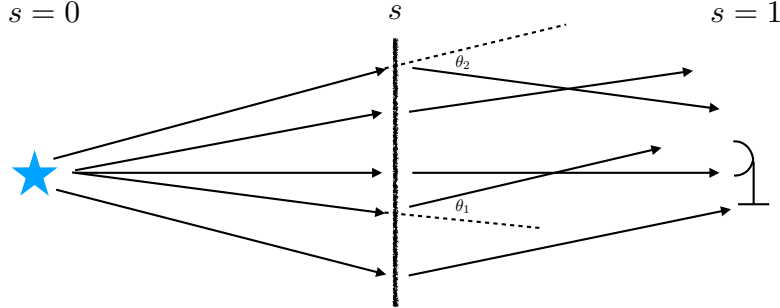


Figure 2.2: A basic diagram of the thin screen scattering geometry, indicating the screen location  $s$  and the scattering angles corresponding to waves scattered in directions  $\theta_1$  and  $\theta_2$ .

where  $\mathbf{v}_{p\perp}$ ,  $\mathbf{v}_{obs\perp}$ , and  $\mathbf{v}_{scr\perp}$  are the transverse velocities of pulsar, observer, and screen, respectively (Cordes & Rickett 1998).

Consider a plane wave from a pulsar incident on a phase-changing screen. The wave will emerge with a corrugated wave front that, if it were imaged with high angular resolution, would be a point source surrounded by a weak halo (Lyne & Graham-Smith 2012). Hill et al. (2003) have shown that for such an image, fixing  $\theta_1 = 0$  and  $\mathbf{v}_{p\perp} \gg \mathbf{v}_{obs\perp}, \mathbf{v}_{scr\perp}$  results in a simple parabolic relationship between  $f_\nu$  and  $f_t$ :

$$f_\nu = \frac{D\lambda^2}{2cv_{p\perp}^2} \frac{s}{1-s} f_t^2 \quad (2.6)$$

where the scintillation arc curvature  $\eta = f_\nu/f_t^2$  is thus

$$\eta = \frac{D\lambda^2}{2cv_{p\perp}^2} \frac{s}{1-s}. \quad (2.7)$$

The more general definition of arc curvature, resulting when a linear scattering structure is inclined by an angle  $\psi$  with respect to  $\mathbf{v}_{eff}$ , is given by

$$\eta = \frac{D\lambda^2}{2c} \frac{s(1-s)}{v_{eff}^2} \sec^2\psi. \quad (2.8)$$

### 2.2.2 Dynamic and Secondary Spectra

Fringes in the dynamic spectrum can be understood as interference between waves scattered by a thin screen. The observer travels relative to the screen along Earth's orbit, and thus sees the fringes vary sinusoidally in frequency and time. This sinusoidal variation appears as pairs of points in the secondary spectrum, producing a scintillation arc (Trang & Rickett 2007). Mathematically, these pairs of points can be expressed as delta functions, which summed together form the secondary spectrum (Cordes et al. 2006):

$$S_2(p, q) = \int \int d\boldsymbol{\theta}_1 d\boldsymbol{\theta}_2 B(\boldsymbol{\theta}_1) B(\boldsymbol{\theta}_2) \delta(p - \bar{p}) \delta(q - \bar{q}) \quad (2.9)$$

where  $B(\boldsymbol{\theta})$  denotes the scattered brightness distribution (or image, as it is often called), and  $p$  and  $q$  are dimensionless delay and fringe frequency (Cordes et al. 2006):

$$p = \frac{2cs}{D(1-s)} f_\nu \quad (2.10)$$

$$q = \frac{\lambda s}{v_{\text{eff}}} f_t. \quad (2.11)$$

The dependence of the secondary spectrum on the scattered brightness distribution, as demonstrated by Eq. 2.9, can be used to model scintillation arcs.

### 2.2.3 Proposed Models

While the basic scintillation arc phenomenon can be explained by making simple assumptions about scattering off a thin screen, the complexity of observed scintillation arcs requires more nuanced and astrophysically motivated modeling.

Several scattered brightness distributions capable of producing scintillation arcs have already been modeled. Cordes et al. (2006) examined brightness distributions ranging from simple cases like point images, elongated 1D images, and images with a point source and extended component, to more astrophysical cases like elliptical Gaussian images and images from power-law inhomogeneity spectra, such as those resulting from Kolmogorov turbulence

in the plasma.. While they managed to rule out point images and elliptical Gaussian images, certain types of scattered brightness distributions—namely, those with a point source and extended component, and those with power-law spectra—remain attractive. Scattered images following a Kolmogorov spectrum are of particular interest because electron density fluctuations in the ISM have been shown to follow such a spectrum over more than 10 orders of magnitude in size scale (Armstrong et al. 1995).

Trang & Rickett (2007) performed a similar investigation by fitting a brightness distribution to a secondary spectrum of the pulsar B1133+16. Their result, a brightness distribution that was elongated and asymmetric, suggests that the ISM scattering responsible for scintillation arcs could be localized in discrete regions of highly anisotropic scattering. Moreover, they suggest that these regions are small, subtending angles of 0.1 to 1 milliarcseconds. Rickett et al. (2011) similarly concluded that the scattered images for scintillation arcs observed in pulsars B0834+06 and B1737+13 were elongated and modulated in power and suggested the corresponding scattering regions might be ancient supernovae remnants.

Walker et al. (2017) have proposed a different astrophysical source for such localized scattering regions: plasma filaments associated with hot main sequence stars. Since the production of scintillation arcs requires scattering regions with plasma pressures much greater than those typical in the ISM, they conjecture these regions are molecular clumps around main sequence stars, and demonstrate that such an association could explain observations of scintillation arcs in several pulsars.

Other modeling attempts have focused on the refractive scattering behavior for various kinds of sheets and lenses. Building on a previous model for refraction through a plasma lens (Pen & King 2012), Pen & Levin (2014) have suggested a model for scattering off of corrugated reconnection sheets that are closely aligned with the line of sight to the pulsar. Their model implies that magnetic reconnection might be a promising physical mechanism for the production of thin plasma sheets in the ISM.

As yet, the only consensus on a physical model for the production of scintillation arcs is that the scattering regions are localized in thin, inho-

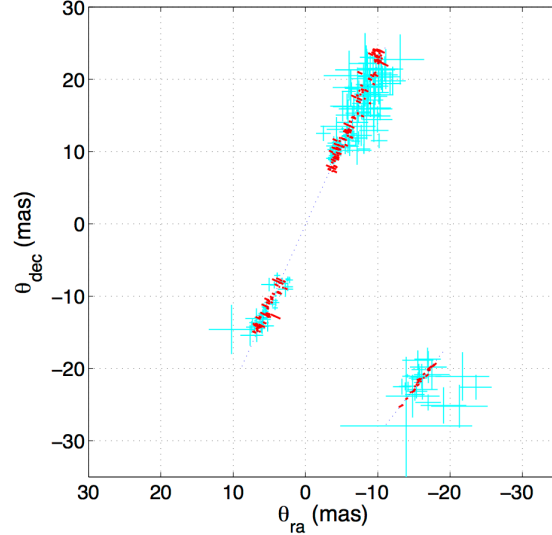


Figure 2.3: The scattered image of the pulsar B0834+06 (Briskin et al. 2010), determined using VLBI and the secondary spectrum of the pulsar. Lower and higher precision astrometric measurements are shown in cyan and red, respectively.

mogeneous screens, somewhere between  $10^3$  km and 10 AU (astronomical unit - referring to the distance between Earth and the Sun) in size (Cordes et al. 2006). This consensus is supported by many scintillation arc observations, but most notably by the astrometric mapping of the pulsar B0834+06 determined by Briskin et al. (2010). Using Very Long Baseline Interferometry (VLBI), Briskin et al. find that the scattered brightness of B0834+06, shown in Fig. 2.3, consists of two components, each highly anisotropic and linear. Their observation provides direct evidence that the scattering regions responsible for scintillation arcs are highly elongated and inhomogeneous.

### 2.3 Key Observational Results

Any model for the production of scintillation arcs benefits from the following observational results that have enhanced our understanding of the arc

phenomenon:

- Scintillation arcs are common: 16 out of 18 observed pulsars had scintillation arcs in an unbiased survey of low dispersion measure pulsars (Stinebring 2007; Stinebring et al. in prep).
- While arc curvatures remain constant up to 20 years and more, the power distribution of a scintillation arc changes on timescales of days to months (Stinebring et al. 2003).
- Arc curvature scales with observing wavelength squared (Hill et al. 2003).
- Arc substructure (such as arclets) translates along the main parabolic arc depending on the pulsar’s proper motion (Hobbs et al. 2005; Rickett 2007).
- Pulsar distance and proper motion, obtained through Very Long Baseline Interferometry, have localized scattering screens for numerous pulsars (e.g., Putney & Stinebring (2006); Brisken (2009); Bhat et al. (2016)).

## 2.4 Purpose of the Thesis

While significant observational and theoretical progress has been made since the discovery of scintillation arcs in 2001, the astrophysical nature of the scattering regions responsible for scintillation arcs remains unknown. While numerous models for the scattering mechanism have been proposed, very few have actually been compared to observations. This thesis lays out the unique model-testing capabilities of the pulsar B1133+16.

One of the first four pulsars discovered, B1133+16 has a number of observational advantages for exploring scintillation arcs. Not only is it located at a close distance of 350 pc (parsecs - about 3.3 light years) from Earth, but its mean flux density at 400 MHz (or S400) is extraordinarily bright at 257 mJy. Its visibility within the declination range of both the Arecibo Observatory and the Low-Frequency Array (LOFAR) allows the pulsar to

be studied over a wide range of radio frequencies. Moreover, B1133+16 has one of the highest known transverse velocities, 640 km/s (Hobbs et al. 2005), allowing it to traverse a vast range of the ISM. With a long (albeit intermittent) history of observation at numerous frequencies, B1133+16 exhibits a unique variety of scintillation behavior, most notably three highly delineated scintillation arcs observable in high frequency data spanning several decades.

Using data taken over five months and three frequencies at the Arecibo Observatory by the Oberlin pulsar group and LOFAR data courtesy of Joris Verbiest, this thesis will examine the capability of B1133+16 for testing models of scintillation arcs in the following chapters:

Chapter 3 will examine whether the variation of B1133+16 scintillation arc curvature measurements is due to Earth’s annual orbit, and whether such annual modulation can be used to extract the location(s) of scattering screen(s). Chapter 4 will lay out the formalism for using arc width measurements to determine the width of a linear scattering image. The frequency dependence of arc width measurements for B1133+16 will be determined. Chapter 5 will examine extensions of the arc width formalism and analysis for testing models for the production of scintillation arcs. Chapter 6 presents my conclusions and remarks on future work.

Understanding the physical origins of scintillation arcs promises important new insights into ISM and scintillation studies. Not only do scintillation arcs imply the existence of discrete, highly elongated, screen-like structures smaller than the majority of structures hitherto studied in the ISM, but they also provide a fruitful avenue for studying and mitigating time-variable delays in arrival time that are crucial for the detection of gravitational waves with a pulsar timing array (Lam et al. 2017).

## Chapter 3

# Annual Arc Curvature Modulation

Scintillation arc curvature measurements have been shown to exhibit annual modulation due to Earth’s rotation around the Sun (Stinebring et al. 2005). Under ideal conditions, measuring such curvature variation lets us unambiguously determine the location of the scattering screen and determine the angle  $\psi$  of the scattering image with respect to the pulsar effective velocity. This chapter lays out the theory behind annual arc curvature variations due to Earth’s orbit, and will determine whether B1133+16 shows such variation.

### 3.1 Theory

The following is based on a formalism developed by Artem Tuntsov at Manly Astrophysics, Australia (Tuntsov 2017). Consider a scattering image that is linear with direction  $\hat{\rho}$ , a 2D vector in the plane of the sky which only varies negligibly as Earth revolves around the Sun. The curvature of a scintillation arc resulting from this scattering image will be

$$\eta = \frac{D\lambda^2}{2c} \frac{s(1-s)}{(\hat{\rho} \cdot \mathbf{v}_{\text{eff}})^2} \quad (3.1)$$

where the effective velocity is given by Eq. 2.5, restated here:

$$\mathbf{v}_{\text{eff}} = (1 - s)\mathbf{v}_{\text{p}\perp} + s\mathbf{v}_{\text{obs}\perp} - \mathbf{v}_{\text{scr}\perp}.$$

For large  $s$  (screen close to Earth), modulation in  $\mathbf{v}_{\text{obs}\perp}$  due to Earth's orbit will cause noticeable variation in  $\mathbf{v}_{\text{eff}}$  and  $\eta$ . The observer velocity changes with Earth's orbit, tracing out an ellipse around a fixed offset:

$$\mathbf{v}_{\text{obs}\perp} = \mathbf{v}_{\odot} + \hat{e}_1 v_1 \cos \phi + \hat{e}_2 v_2 \sin \phi \quad (3.2)$$

where  $\mathbf{v}_{\odot}$  is the velocity of the Solar System barycentre (roughly the velocity of the Sun),  $\hat{e}_1$ ,  $\hat{e}_2$ ,  $v_1$ ,  $v_2$  are the directions and magnitudes of the major and minor axes of the ellipse, and  $\phi$  is the eccentric anomaly, which defines the angular position of Earth in its orbit.

The impact of elliptical modulation in  $\mathbf{v}_{\text{obs}\perp}$  is demonstrated by solving for the inverse curvature:

$$\frac{\lambda^2 D}{2c\eta} = \frac{(\hat{\rho}\mathbf{v}_{\text{eff}})^2}{s(1-s)}.$$

Expanding, we find

$$\begin{aligned} \frac{\lambda^2 D}{2c\eta} = & \frac{(v_{SL}^\rho)^2}{s(1-s)} + \frac{2\hat{\rho}(v_{SL}^\rho)}{(1-s)}v_1 \cos \phi + \frac{2\hat{\rho}(v_{SL}^\rho)}{(1-s)}v_2 \sin \phi \\ & + \frac{s}{2(1-s)}(v_1^2 + v_2^2) + \frac{s}{2(1-s)}(v_1^2 - v_2^2) \cos 2\phi \quad (3.3) \end{aligned}$$

where

$$v_{SL}^\rho \equiv \hat{\rho}(s\mathbf{v}_{\text{p}\perp} - \mathbf{v}_{\text{scr}\perp})$$

(see Appendix A). Eq. 3.3 has four main coefficients—a constant term and three oscillatory terms,  $\cos \phi$ ,  $\sin \phi$ , and  $\cos 2\phi$ —which can be fit to a series of curvature measurements to constrain four unknown variables— $s$ ,  $\hat{\rho}$ , and the two components of  $\mathbf{v}_{\text{scr}\perp}$ . Thus in an ideal case, annual curvature modulation could be used to determine both the screen location and transverse velocity. Eq. 3.3 also demonstrates that a plot of inverse curvature as a function of  $\phi$  follows a double-humped curve over the course of a full Earth orbit (Tuntsov 2017).

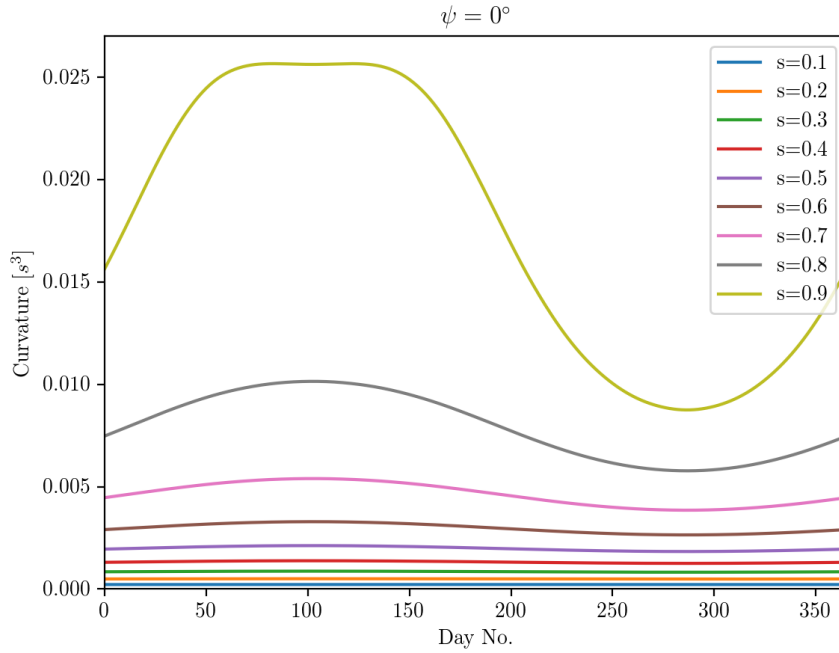


Figure 3.1: Expected curvature modulation for B1133+16 over a year long cycle beginning on MJD (Modified Julian Day number) 57083, assuming the scattering image is aligned with  $\mathbf{v}_{\text{eff}}$  and the screen is effectively stationary ( $\mathbf{v}_{\text{scr}\perp} \approx 0$ ). The observing frequency was taken to be 1450 MHz.

For the extreme case in which the scattering image is aligned with  $\mathbf{v}_{\text{eff}}$  ( $\hat{\rho} \cdot \hat{v}_{\text{eff}} = 1$ ) and the screen is effectively stationary ( $\mathbf{v}_{\text{scr}\perp} \approx 0$ ), Eq. 2.5 becomes

$$\mathbf{v}_{\text{eff}} = (1 - s)\mathbf{v}_{\text{p}\perp} + s\mathbf{v}_{\text{obs}\perp}$$

and  $\eta$  (Eq. 3.1) can be simply modeled using known measurements of  $D$  and the components of  $\mathbf{v}_{\text{p}\perp}$  and  $\mathbf{v}_{\text{obs}\perp}$ . Fig. 3.1 shows the expected annual curvature modulation for B1133+16 under these assumptions for nine screen locations.

## 3.2 Observational Data and Methods

To determine whether B1133+16 displays annual curvature modulation, we used eight secondary spectra, taken from dynamic spectra measured at Arecibo Observatory between March and June 2015 at 1450 MHz with 160 MHz bandwidth. Scintillation arcs are narrow and well-resolved at this frequency. As shown in Fig. 3.2 and Fig. 3.3, the first secondary spectrum, measured on 2015 March 2, displays three discrete scintillation arcs, while the last secondary spectrum, measured on 2015 June 6, only contains one visible arc.

The curvatures of the scintillation arcs were obtained using Sam McSweeney’s `veff` package (McSweeney 2017), which determines arc curvatures using the function `parabfit`, loosely based on the Hough transform, a feature extraction technique used in image processing. For every point in a secondary spectrum, the function determines a range of curvatures that could describe a parabola intersecting that point. The function then determines the number of pixels that fit a given parabola and curvature range. The result of the transform is a plot depicting the average pixel intensity for all of the iterated curvatures. Thus peaks in average intensity vs. curvature correspond to the most likely curvature values.

One of the plots produced by our analysis is shown in Fig. 3.4. The three peaks in the plot correspond to three distinct arcs detected in the secondary spectrum. Since each arc has some width, there is a spread in the possible curvature values for each arc, resulting in approximately Gaussian peaks in the plot. Using a non-linear least squares fit, we determined the Gaussian mean and standard deviation of each peak, corresponding to the best fit curvature and uncertainty for each arc.

Comparison with the annual modulation model required the pulsar’s proper motion, distance from Earth, and position on the sky, along with the observer’s barycentric, transverse velocity. The pulsar parameters were taken from the pulsar database `psrcat` (Manchester et al. 2005). The observer’s barycentric velocities for a full annual cycle around the Sun were determined using the PyAstronomy `baryCorr()` function (Czesla 2017). In-

stead of using Artem Tuntsov's notation of  $\hat{\rho}$  to describe the position of the scattering screen with respect to  $\mathbf{v}_{\text{eff}}$ , we used the angle  $\psi$  to describe the angle between the scattering screen and the effective velocity, with the curvature defined accordingly (see Eq. 2.8).

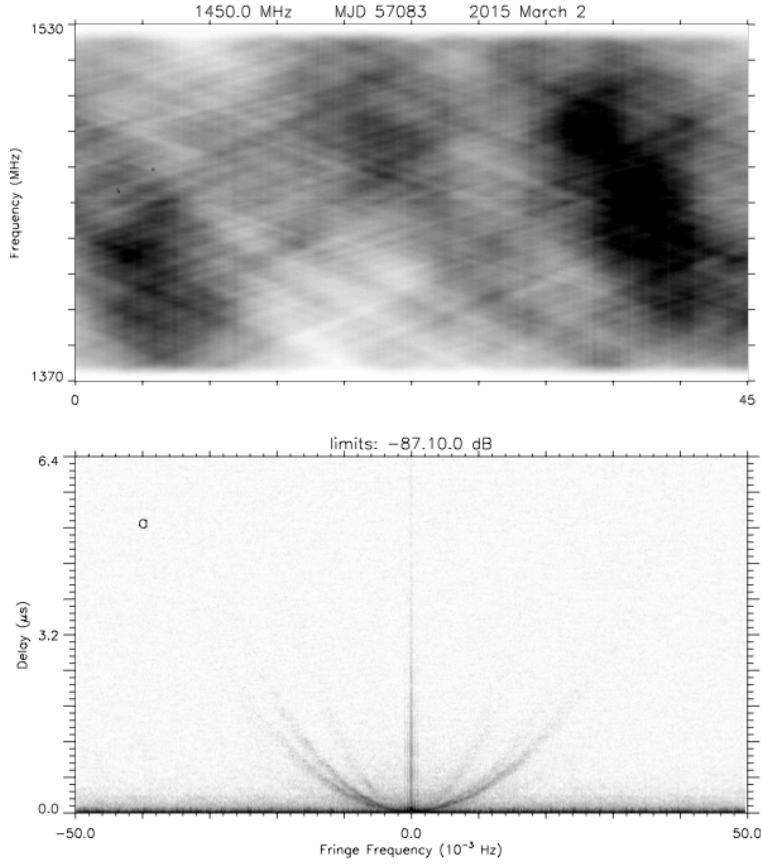


Figure 3.2: Dynamic and secondary spectra for B1133+16, displaying three distinct scintillation arcs. The spectra were taken on 2015 March 2 at Arecibo Observatory at 1450 MHz. Figure courtesy of Dan Stinebring.

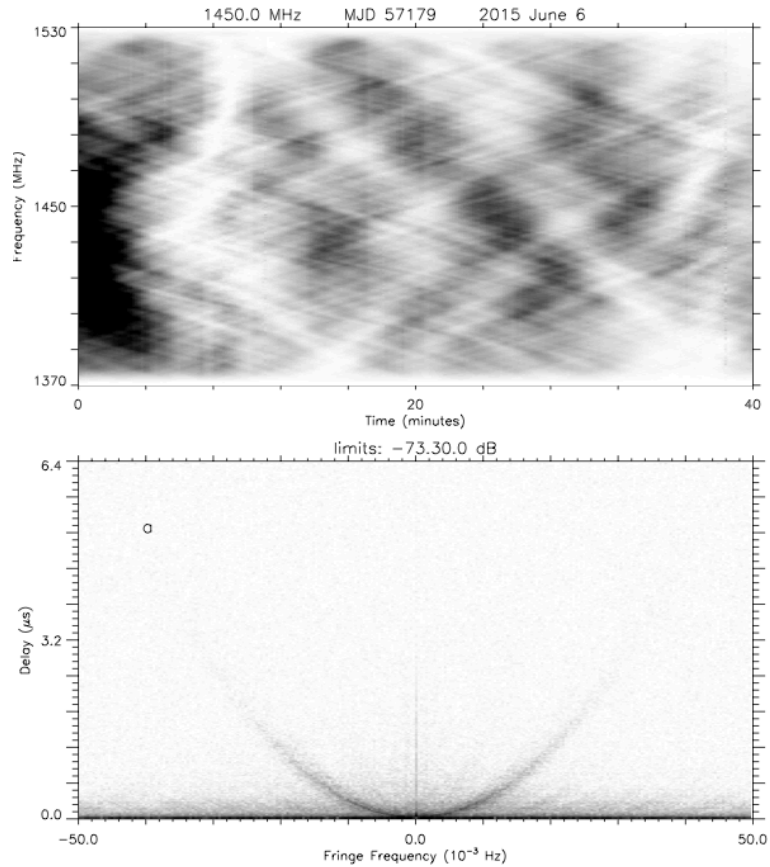


Figure 3.3: Dynamic and secondary spectra for B1133+16, displaying a single distinct scintillation arc. The spectra were taken on 2015 June 6 at Arecibo Observatory at 1450 MHz. Figure courtesy of Dan Stinebring.

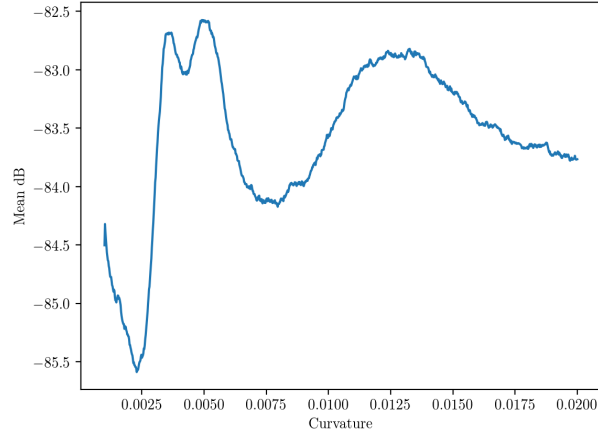


Figure 3.4: Average intensity vs. curvature plot produced by running `veff` on a secondary spectrum of B1133+16. The three peaks correspond to the curvatures that matched the largest number of pixel bins (represented here in mean dB, the bin intensity).

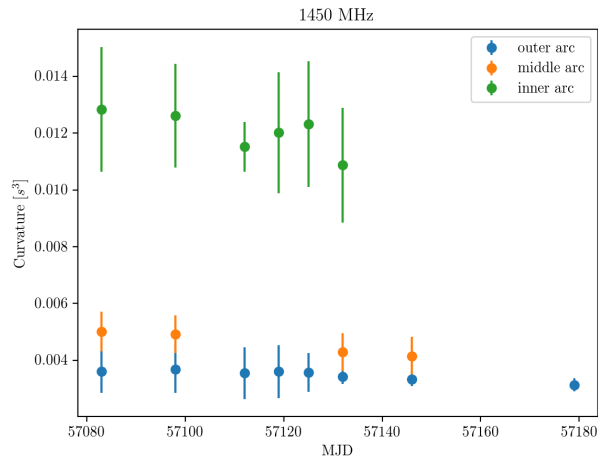


Figure 3.5: Measured curvatures for three distinct scintillation arcs detected in secondary spectra for B1133+16 over a 96 day span of observations at 1450 MHz. Curvatures for the outer, middle, and inner arcs are shown in blue, orange, and green, respectively.

### 3.3 Results

The measured curvatures over the full 96 day span of observations are shown in Fig. 3.5. Curvatures for three distinct arcs are shown; the only arc to remain visible in every observation is the outermost arc, corresponding to the lowest curvature. The curvature uncertainty is disproportionately high for the innermost arc because it had the faintest intensity for almost every observation in which it was visible. The measured curvatures show no convincing variation. Such constant curvature usually implies that the screen location  $s$  is low, meaning  $\mathbf{v}_{p\perp}$  dominates  $\mathbf{v}_{\text{eff}}$  (Eq. 2.5). However, it is possible that B1133+16 has such a high velocity that  $\mathbf{v}_{\text{eff}}$  is dominated by  $\mathbf{v}_{p\perp}$  regardless of screen location.

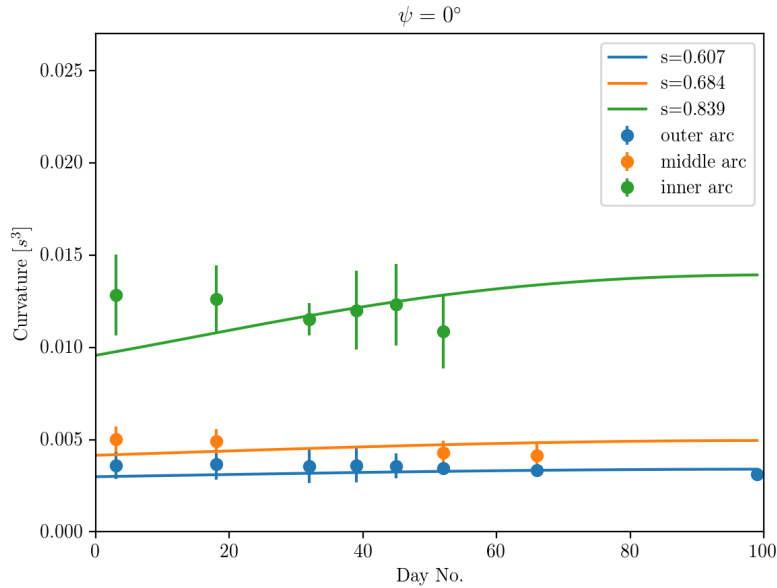


Figure 3.6: Measured curvatures and the corresponding curvatures for best values of  $s$  determined with a nonlinear least squares fit. The fit was calculated using the annual modulation model described in Section 3.1, under the assumption that the  $\mathbf{v}_{\text{scr}} \approx 0$  and  $\psi = 0^\circ$ .

To test this possibility, we determined the best values of  $s$  for each arc using a nonlinear least squares fit at five values of  $\psi$ :  $0^\circ$ ,  $20^\circ$ ,  $40^\circ$ ,  $60^\circ$ , and  $80^\circ$ , for the case in which  $\mathbf{v}_{\text{scr}\perp} \approx 0$ . Fig. 3.6 through Fig. 3.10 show the measured and fitted curvatures for the 96 day observation period at each value of  $\psi$ , along with the fitted  $s$  values. In general, higher values of  $\psi$  resulted in lower best-fit  $s$  values and lower expected curvature modulation. Unfortunately, each  $\psi$  and  $s$  fit seems equally suitable for the outer and middle arcs, indicating that  $\mathbf{v}_{\text{p}\perp}$  is so high that there is no significant curvature modulation. For the innermost arc, the fitted curvature shows modulation on the order of  $0.005 \text{ s}^3$  for  $\psi = 0^\circ$  and  $\psi = 20^\circ$ , which decreases to almost no modulation for  $\psi = 80^\circ$ . The measured curvatures of the innermost arc are relatively constant, suggesting that  $\psi = 0^\circ$ , and possibly  $\psi = 20^\circ$ , can be ruled out for that arc.

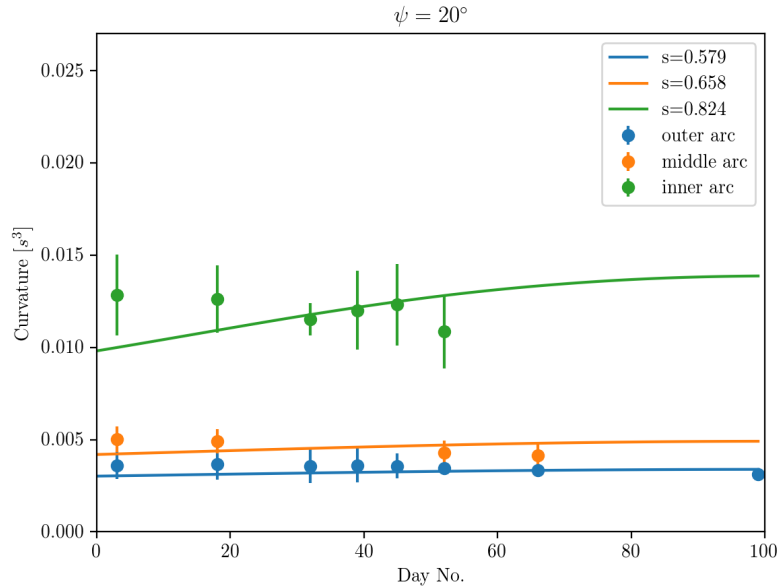


Figure 3.7: Measured and fitted curvatures, as in Fig. 3.6, for  $\psi = 20^\circ$ .

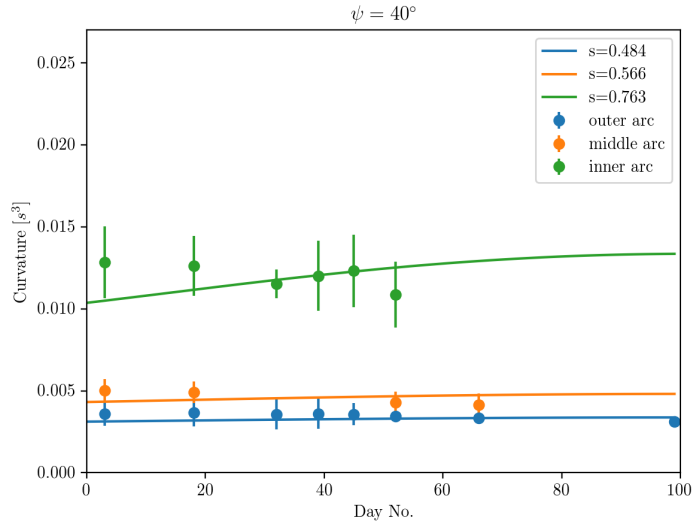


Figure 3.8: Measured and fitted curvatures, as in Fig. 3.6, for  $\psi = 40^\circ$ .

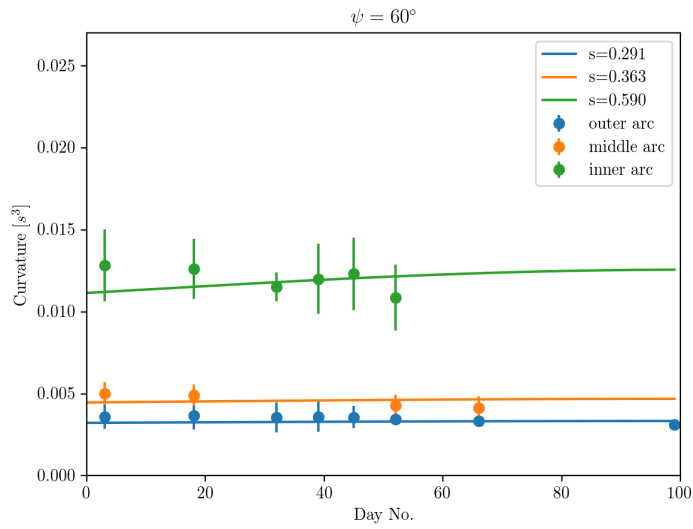


Figure 3.9: Measured and fitted curvatures, as in Fig. 3.6, for  $\psi = 60^\circ$ .

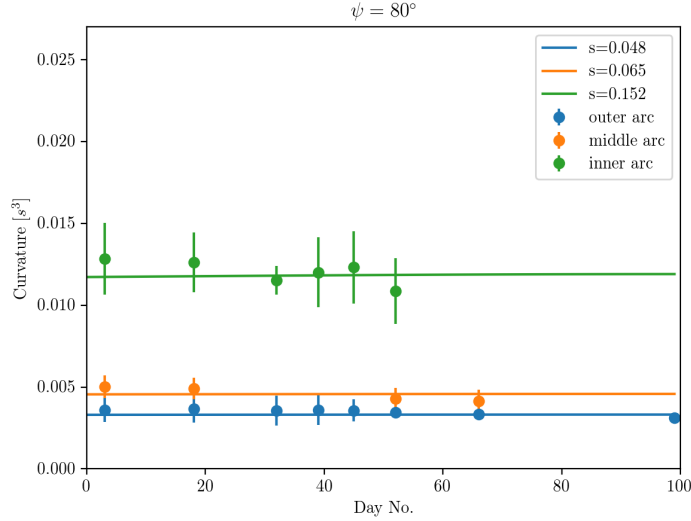


Figure 3.10: Measured and fitted curvatures, as in Fig. 3.6, for  $\psi = 80^\circ$ .

### 3.4 Discussion

We see no statistically significant evidence that B1133+16 shows annual curvature modulation. Fitting the annual modulation model to the measured curvatures, assuming  $\mathbf{v}_{\text{scr}} \approx 0$  (which is reasonable given how fast the pulsar travels transversely), yields a range of possible  $s$  and  $\psi$  values for each scintillation arc:  $0.15 < s < 0.84$  and  $0^\circ < \psi < 80^\circ$ . This range of possible screen locations and inclination angles covers a wide range of physical situations: any of the screens might be very close to the pulsar and closely aligned with  $\mathbf{v}_{\text{eff}}$ , or might be very far from the pulsar and highly inclined with respect to  $\mathbf{v}_{\text{eff}}$ . The best-fit  $s$  values also raise the possibility that the outer and middle arcs correspond to two screens within a distance of  $s = 0.1$  (35 pc) apart. However, an independent method of determining  $\psi$  is necessary to narrow down the value of  $s$  for each arc. Overall, the small magnitude of expected curvature modulation suggests that the velocity of B1133+16 dominates  $\mathbf{v}_{\text{eff}}$  over the orbital modulation of  $\mathbf{v}_{\text{obs}\perp}$ .

B1133+16 has too high a velocity to detect annual curvature modulation

using our current methods. Is it possible to get higher precision curvature measurements? Any curvature measurement is limited in precision by the width of the scintillation arc. However, `parabfit` is additionally limited because it averages the pixel intensities when it bins them into a distribution for different curvature fits, which might effectively smear out the detected arc, increasing the curvature uncertainty and making fainter arcs more difficult to detect.

For example, see the secondary spectrum taken at 327 MHz in Fig. 3.11 and the corresponding `parabfit` output in Fig. 3.12. At least two scintillation arcs are visible in the secondary spectrum, both of similar width. The average intensity plot, by contrast, only has one highly defined peak, corresponding to the outer, darkest arc. There is a second peak in the average intensity plot, but it is extremely broad and double-humped. Examining the secondary spectrum, there is little reason to expect curvature measurements for the two arcs to have significantly different uncertainties, but since `parabfit` is intrinsically limited by the average intensity of each arc, it is incapable of precisely determining a curvature for the inner, fainter arc. For this secondary spectrum, it is possible that performing curvature fits through another method could produce better results than `parabfit`.

While B1133+16 is too fast for us to currently detect annual curvature modulation, other, slower pulsars are likely better candidates for this kind of analysis. Annual curvature modulation has already been used to determine the scattering screen location for B1929+10, which has the much slower transverse velocity of 175 km/s (Kirsten et al. 2015). However, examining B1133+16 arc curvatures over a longer time span could yield interesting results. Are the curvatures always constant, or do they go through periods of noticeable modulation? If so, such modulation could reveal more details about the scattering screen.

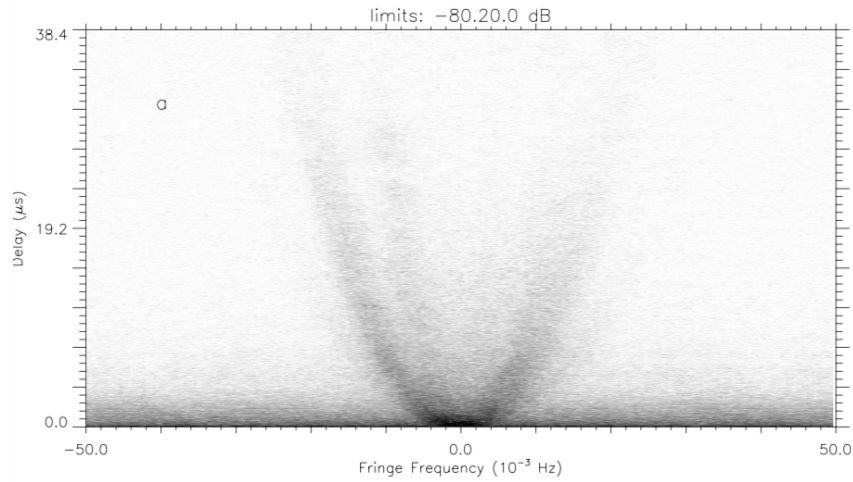


Figure 3.11: Secondary spectrum for B1133+16 at 327 MHz, taken on MJD 57058. At least two scintillation arcs are visible.

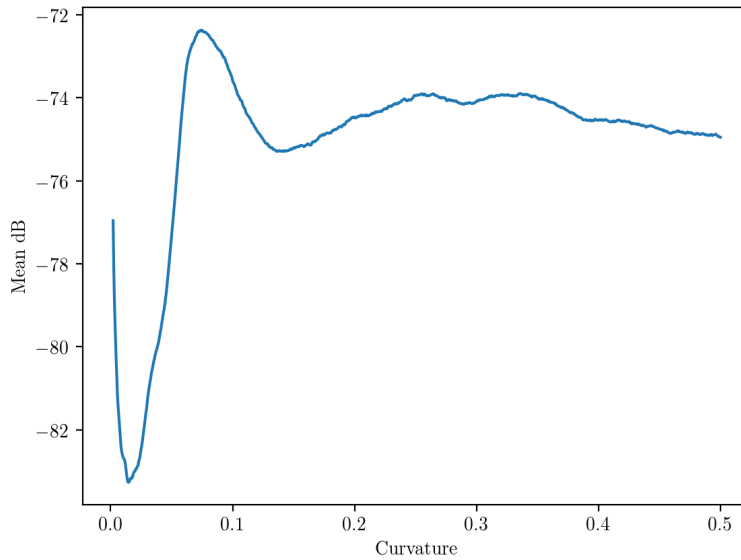


Figure 3.12: Average pixel intensity vs. curvature for the secondary spectrum taken on MJD 57058 at 327 MHz, shown above.

## Chapter 4

# The Frequency Dependence of Scintillation Arc Widths

The shape and behavior of a pulsar's scattered image depends on the details of the screen through which it was scattered. One method of modeling scintillation arcs assumes a certain screen geometry and simulates the resultant image of a pulsar viewed through that screen. The behavior of the scattered image with observing frequency can then be used as a predictive test. This chapter lays out the theoretical relationship between scintillation arc width and the width of a linear scattered image. The frequency dependence of scintillation arc widths and the corresponding image width is determined for B1133+16.

### 4.1 Determining the Width of a Scattered Pulsar Image

Consider again the scenario described in Section 2.2.1: a scattered pulsar image consisting of a point source surrounded by a weak halo (Hill et al. 2003). For interference between a point located at  $\boldsymbol{\theta}_1 = 0$  (the pulsar location) and a point located at  $\boldsymbol{\theta}_2 = \theta_{2,x}$ , where  $\mathbf{v}_{\text{eff}}$  is taken to be in the  $\theta_x$

direction, the fringe frequency is given by

$$\begin{aligned} f_t &= \frac{1}{\lambda_s} \boldsymbol{\theta}_2 \cdot \mathbf{v}_{\text{eff}} \\ &= \frac{1}{\lambda_s} \theta_{2,x} v_{\text{eff}}, \end{aligned} \tag{4.1}$$

where  $s$  indicates the screen location, and  $\lambda$  is the observing wavelength. The correspondence between an interval in  $f_t$  and points on the sky is thus

$$\Delta\theta_{2,x} = \frac{\lambda_s}{v_{\text{eff}}} \Delta f_t. \tag{4.2}$$

It thus follows from the simple thin screen analysis laid out in Chapter 2 that changes in fringe frequency, observed in the secondary spectrum, directly correspond to the angular width of the pulsar image. Moreover, if its only frequency dependence arises from  $f_t$ , then that angular width is indirectly proportional to observing frequency (Hill et al. 2003).

Modeling efforts over the past decade have shown that scintillation arcs likely arise from thin, highly elongated pulsar images (see Section 2.2.3). Consider such a scattered image, of width  $w$ , tilted linearly at an angle  $\psi$  with respect to  $\mathbf{v}_{\text{eff}}$ . The image geometry is shown in Fig. 4.1. A simple analysis demonstrates that

$$\Delta\theta_x = w \sin \psi. \tag{4.3}$$

For interference between a point at  $\boldsymbol{\theta}_1 = 0$  and a point at  $\boldsymbol{\theta}_2$ , we will again arrive at Eq. 4.1; so, for this particular image geometry, the image width  $w$  scales inversely with observing frequency:

$$w \propto \Delta\theta_x \propto \frac{\Delta f_t}{\nu}. \tag{4.4}$$

Thus the fringe frequency width of a scintillation arc,  $\Delta f_t$ , can be used as an indirect measure of the scattered image width, and is expected to decrease with observing frequency as  $\nu^{-1}$  if the image itself is frequency independent. Any frequency dependence of the image width, which might be expected in several scenarios, will affect the measured width according to Eq. 4.4. Additionally, if  $\psi$  is independently determined (e.g. through the measurement of

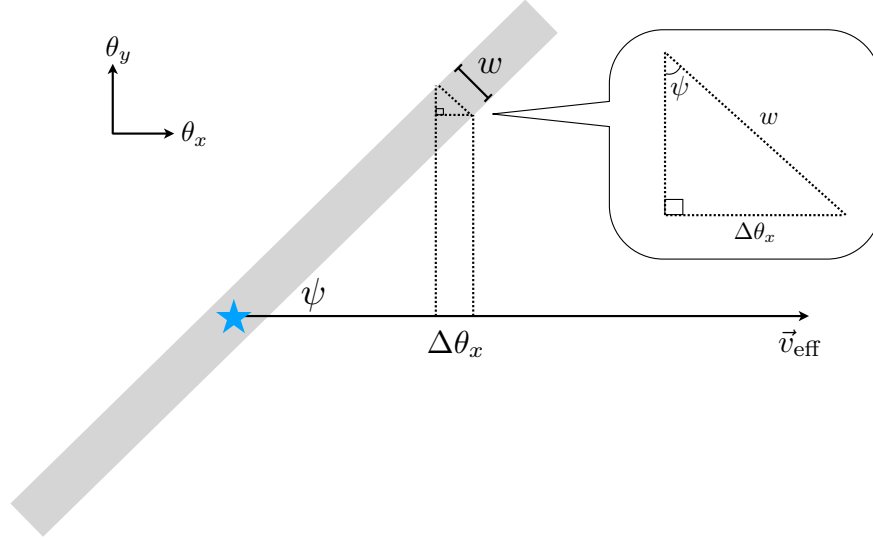


Figure 4.1: Geometry of a linear, highly elongated pulsar image tilted at an angle  $\psi$  with respect to  $\mathbf{v}_{\text{eff}}$ , which is aligned with the  $\theta_x$  axis. The pulsar is depicted in blue and the scattered image in gray (not to scale). The relevant widths  $\Delta\theta_x$  and  $w$  are also shown. In this geometry,  $w$  does not depend on observing frequency.

annual curvature modulation described in Chapter 3), then the image width can be determined from  $\Delta\theta_x$ .

For  $\psi = 0^\circ$ , the above analysis would fail because  $\Delta\theta_x = 0$ . Alternatively, one could consider the delay, given by Eq. 2.6, but which can also be stated as

$$f_\nu = \frac{D(1-s)}{2cs}(\theta_2^2 - \theta_1^2) \quad (4.5)$$

(Hill et al. 2003). For  $\theta_1 = 0$ ,  $f_\nu$  subtends a circle in the  $\theta_x$ - $\theta_y$  plane. For small  $w$ ,  $f_\nu$  intersects the scattering image approximately linearly, suggesting that  $\Delta f_\nu$  also directly corresponds to the image width.

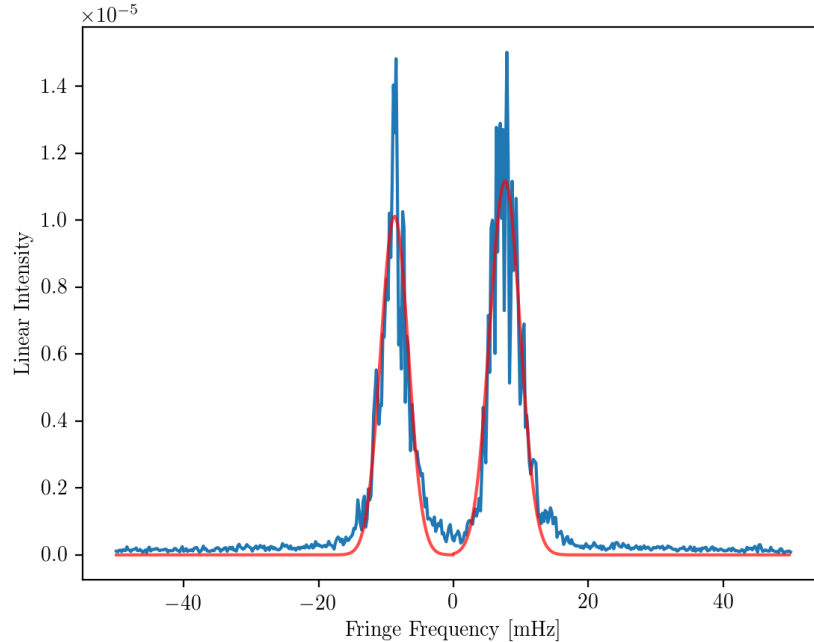


Figure 4.2: A cross-cut of the linear pixel intensity averaged over 20 delay rows, taken from the secondary spectrum of B1133+16 on MJD 57090 at 327 MHz. The fitted Gaussian functions are shown in red.

## 4.2 Frequency Dependence of B1133+16 Arc Widths

### 4.2.1 Observational Data and Methods

To examine the frequency-dependent behavior of B1133+16 arc widths, we used secondary spectra taken at Arecibo Observatory over a five month period in early 2015. For maximum uniformity of comparison we concentrated on data obtained within a two week period over three frequencies: two secondary spectra taken on MJD 57090 at 327 and 432 MHz, and one secondary spectrum taken on MJD 57083 at 1450 MHz (all with 160 MHz bandwidth). We also obtained data taken on MJD 57094 at 125 MHz with the Low-Frequency Array (LOFAR), courtesy of Joris Verbiest, Stefan Osłowski, and

Lars Künkel (University of Bielefeld, Germany).

To measure the scintillation arc width in fringe frequency,  $\Delta f_t$ , cross-sectional cuts of the secondary spectrum were taken at evenly spaced delay intervals, where each cut averaged the pixel intensity over 20 delay bins. An example of the resulting intensity vs. fringe frequency distribution is shown in Fig. 4.2. Each scintillation arc corresponds to a peak in intensity. Using a non-linear least squares fit, we determined the Gaussian mean and standard deviation of each peak, corresponding to the arc width and uncertainty, respectively. The measured arc widths were averaged to give a single value of width at each frequency, and a weighted linear least squares fit was performed on the average  $f_t$  width as a function of observing frequency.

### 4.2.2 Results

The measured arc widths in  $f_t$  for a range of delay values are shown at 125, 327, 432, and 1450 MHz in Fig. 4.3 through Fig. 4.6. At 125 MHz the scintillation arc was one-sided and varied noticeably with delay. At 327 and 432 MHz, the arc width remained relatively constant over delay, but the arc was consistently wider in positive  $f_t$  (corresponding to the right-hand side of a secondary spectrum) than in negative  $f_t$  (the left-hand side of a secondary spectrum). The secondary spectrum at 1450 MHz displayed three distinct arcs, but only the widths of the middle arc are shown in Fig. 4.6. These arc widths were also relatively constant, but the negative  $f_t$  arc was consistently wider than the positive  $f_t$  arc.

The average width in  $f_t$  as a function of observing frequency is shown in Fig. 4.7. A weighted linear least squares fit to the average widths at the four frequencies yielded  $f_t \propto \nu^{-0.8 \pm 0.1}$ .

The average width at 125 MHz appears anomalously low given this power law fit. The reason lies in the secondary spectrum, shown in Fig. 4.8. The scintillation arc intensity is dominated by a thin concentration of power in the second quadrant of the secondary spectrum, which lies within the region delineated by the expected curvature of a scintillation arc scaled down from 327 MHz (shown in blue). A cross-cut of the linear intensity at this frequency, shown in Fig. 4.9, demonstrates that the thin stripe of power

in the second quadrant dominates the more diffuse background power of the scintillation arc, resulting in an anomalously low arc width at this frequency.

Combining the measured widths at 125, 327, 432, and 1450 MHz with Eq. 4.4 yields  $\Delta\theta_x \propto \nu^{-1.8 \pm 0.1}$  and thus that  $w \propto \nu^{-1.8 \pm 0.1}$ . However, for the image geometry laid out in Section 4.1, the expected frequency scaling is  $\nu^{-1}$ . This discrepancy suggests that the key assumption of the assumed image geometry, that the image width does not inherently depend on observing frequency, is wrong. Rather, the image width must depend on observing frequency.

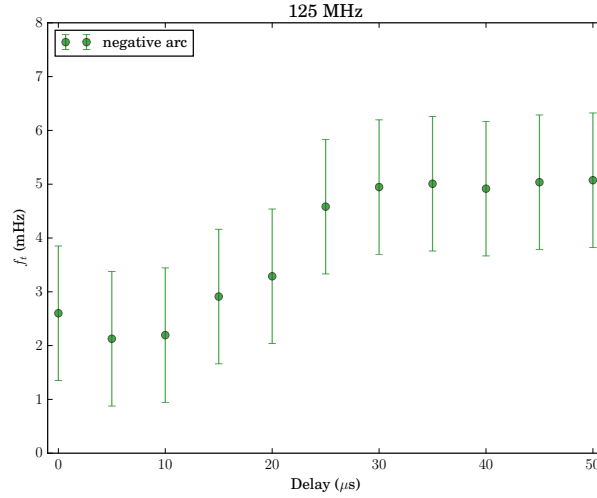


Figure 4.3: Measured arc widths in  $f_t$  vs. delay in  $\mu\text{s}$  at 125 MHz. The widths of the negative  $f_t$  arc are shown in green. The scintillation arc was one-sided in the negative  $f_t$  quadrant of the secondary spectrum.

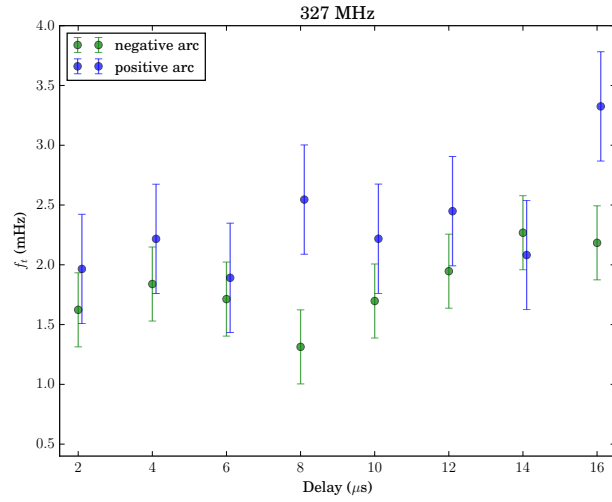


Figure 4.4: Measured arc widths vs. delay at 327 MHz. The widths of the negative  $f_t$  arc are shown in green, and the widths of the positive  $f_t$  arc are shown in blue.

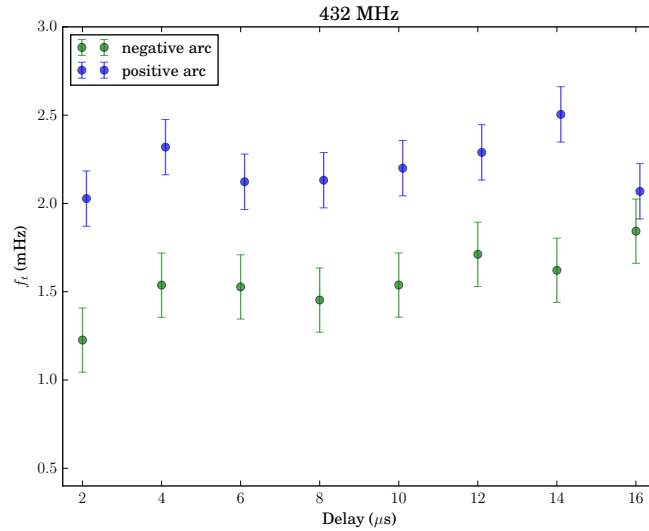


Figure 4.5: Measured arc widths vs. delay at 432 MHz. The arc widths are labeled as in Fig. 4.4.

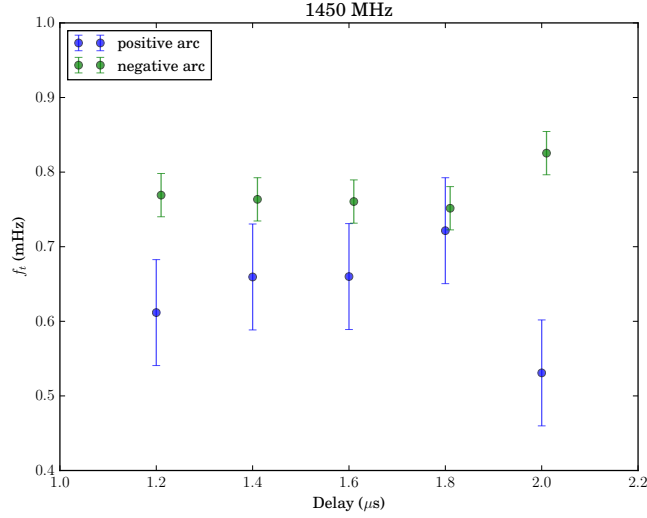


Figure 4.6: Measured arc widths vs. delay for the middle arc at 1450 MHz. The arc widths are labeled as in Fig. 4.4.

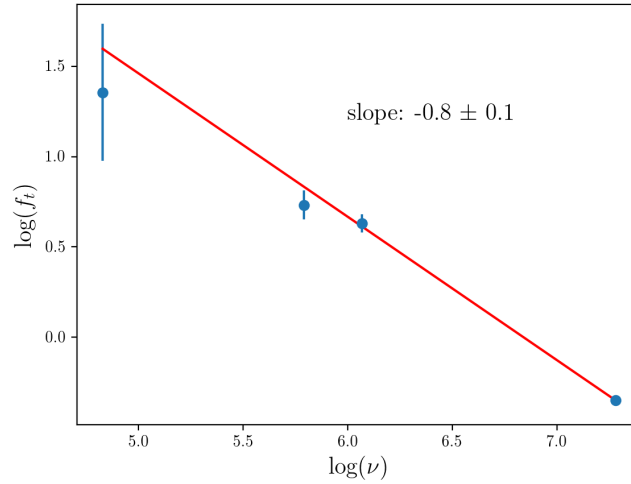


Figure 4.7: Average width in  $f_t$  as a function of observing frequency. The y-axis is  $\log(f_t)$ , while the x-axis shows  $\log(\nu)$ . The average widths are shown in blue. A weighted linear least squares fit on the widths is shown in red, corresponding to a slope of  $-0.8 \pm 0.1$ .

### 4.3 Discussion

The results can be summarized as follows:

1. The scintillation arc observed on MJD 57083 is narrower in positive  $f_t$  and wider in negative  $f_t$ . Seven days later, the situation is reversed.
2. The secondary spectrum at 125 MHz displays a thin, one-sided arc superposed on a diffuse background of power.
3. At all four observing frequencies, the cross-cut intensity of the scintillation arcs as a function of  $f_t$  can be described by a Gaussian distribution (or sum of Gaussian distributions).
4. The scintillation arc widths in  $f_t$  are constant as a function of delay.
5. The  $\Delta f_t$  width decreases with observing frequency as  $\nu^{-0.8 \pm 0.1}$ , suggesting that the angular width of the pulsar image  $\Delta\theta_x$  scales as  $\nu^{-1.8 \pm 0.1}$ .

Asymmetric scintillation arcs have been observed on numerous occasions in pulsars such as PSR 0355+55 and 0834+06. The physical cause of asymmetric arcs is still unknown. It is unusual that at 1450 MHz on MJD 57083, B1133+16 displays a scintillation arc that is wider in negative  $f_t$ , and seven days later displays an arc that is wider in positive  $f_t$ . A convincing model for this asymmetry has not been put forward. Perhaps the power in the arc “travels” from negative to positive  $f_t$  over time, as observed for scintillation arclets in Hill et al. (2005).

The anomalously thin arc observed at 125 MHz is another example of asymmetry in our observed secondary spectra. In this case, such asymmetry could indicate that different observing frequencies are capable of probing different scales of a scattering screen. A 1450 MHz observation probes a smaller angular section on the sky than a 125 MHz observation, making it sensitive to different scattering features. Although the scattering features giving rise to scintillation arcs are not known, one possible feature might consist of inhomogeneous regions of dense and diffuse plasma. An observation at low

frequency might sweep through these regions, producing a secondary spectrum that contains both a diffuse background and a sharp, arc-like feature, as observed at 125 MHz.

Regardless of asymmetry in the distribution of power between positive and negative  $f_t$  arcs, the distribution of power within the arcs at every frequency consistently follows a Gaussian distribution. While such a result seems innocuous, it actually poses an interesting question about the possible mechanism producing these scintillation arcs. The power distribution within scintillation arcs produced by scattering off of an isotropic Kolmogorov screen is predicted to consist of a sharp, outer parabolic boundary, with intensity falling off towards the center of the secondary spectrum (Cordes et al. 2006). The inconsistency of this prediction with our observation of Gaussian power distributions within the arcs suggests that scattering by an isotropic Kolmogorov screen is not applicable to our observations of B1133+16.

A scattering model consistent with our data will also need to account for the constancy of the arc widths over delay. Is such constancy actually to be expected? What does it suggest about the scattering mechanism?

One clue to the nature of the scattering mechanism lies in the observed frequency dependence of the arc widths. Our measured arc widths suggest that for B1133+16, the image width  $w(\nu) \propto \nu^{-0.8 \pm 0.1}$ , i.e., the pulsar’s scattered image appears wider at lower observing frequencies. A scattered image independent of observing frequency is thus ruled out for this pulsar. Furthermore, the frequency dependence of  $\Delta\theta_x \propto \nu^{-1.8}$  is suggestively close to the  $\nu^{-2}$  dependence of the scattering angle expected in a plasma.

Our successful measurement of the arc width frequency dependence for B1133+16 suggests a new quantitative method for testing models. Much model testing up to this point has been an elaboration on the basic question: “Does my predicted scintillation arc look like my observed scintillation arc?” Extensive quantitative predictions, based on particular scattering models, have not been published. Our analysis suggests that a useful scattering model should not only predict qualitative features, such as Gaussian distributed power within the arcs, but should also make quantitative pre-

dictions about the frequency dependence of the arc widths.

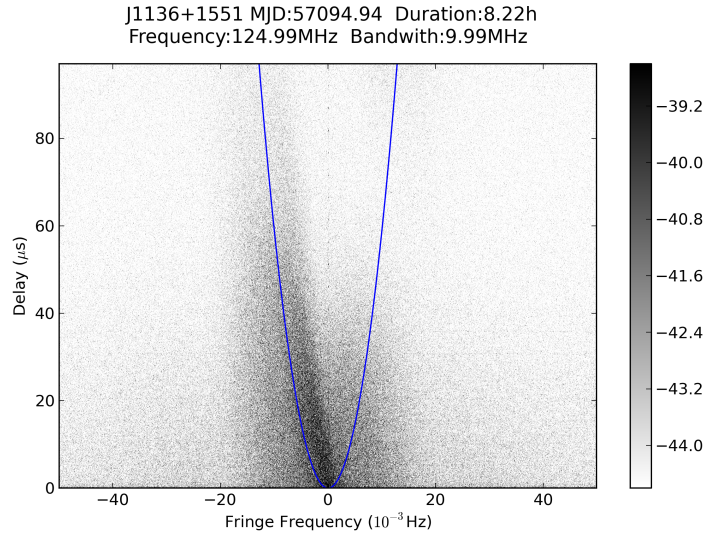


Figure 4.8: The secondary spectrum of B1133+16 on MJD 57094 at 125 MHz. The curvature measured at 327 MHz on MJD 57090, re-scaled to 125 MHz, is shown in blue. Figure courtesy of Lars Künkel.

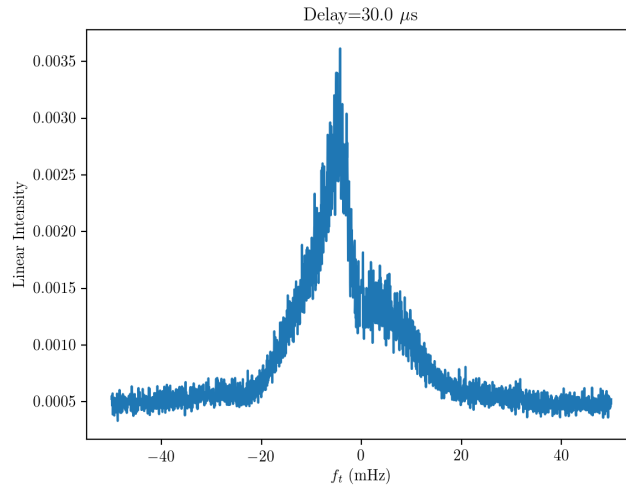


Figure 4.9: The linear intensity cross-cut of the secondary spectrum shown in Fig. 4.8 at a delay of 30.0 μs.

## Chapter 5

# Exploring Models with Arc Width Analysis

The frequency dependence of scintillation arc widths can be used as a method of testing models for the production of scintillation arcs. However, in order to implement such a test, models must first make predictions about the frequency dependence of arc widths. Moreover, the mechanism for broadening an arc at various frequencies depends on the nature of the model. Here we suggest some basic scattered brightness models to explore, and examine the mechanism for broadening an arc in one such model by extracting secondary spectra from an assumed scattered image. In particular, I discuss the viability of a 1D model for B1133+16.

### 5.1 A Collection of Simple Models

Likely models for scattered pulsar images that produce scintillation arcs have already been suggested by fitting brightness distributions to secondary spectra. Such work has demonstrated that scintillation arcs likely arise from highly elongated pulsar images that are modulated in power, and may even be essentially one-dimensional perpendicular to the line of sight (Trang & Rickett 2007).

Six basic scattered image models are shown in Fig. 5.1. Models (a),

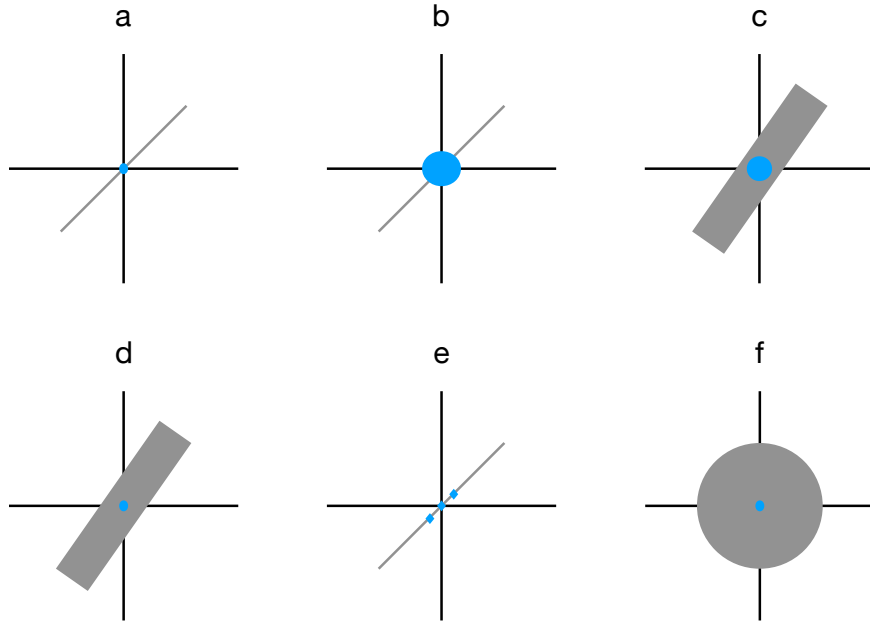


Figure 5.1: Six basic scattered image models. Models (a) and (b) are a highly elongated, 1D pulsar image with a bright, point-like core and a bright, broadened core, respectively. Models (c) and (d) are a broad, elongated image with a bright, broad core and a bright, point-like core, respectively. Model (e) is an elongated, 1D pulsar image with 1D bright “patches,” and model (f) is a bright, point-like core with a broad, scattered halo.

(b), and (e) are variations on a highly elongated, 1D pulsar image with a bright, point-like core (a), a bright, broadened core (b), and a collection of 1D bright “patches” (e). Models (c) and (d) are variations on a highly elongated, broadened pulsar image with a bright, broadened core (c) or a bright, point-like core (d). Model (f) is essentially the image model suggested in Hill et al. (2003): a bright, point-like core and a broad, scattered halo.

Each of these models can be explored in a number of variations. For example, the brightness distribution for model (a) might be a delta function at the core and a power-law extending along the wings, or it might be a

Gaussian function at the core and an exponential function along the wings. Furthermore, each model might produce frequency-dependent arc widths via slightly different mechanisms. In one model, scintillation arcs might broaden at lower frequencies by simply “merging” together or overlapping in the secondary spectrum. In another model, the arcs might broaden as a natural consequence of the plasma frequency dependence; i.e., the image itself broadens out at lower frequencies. Regardless of the mechanism, each model should be able to predict the behavior of the scintillation arc width as a function of frequency.

As discussed in Chapter 2, previous theoretical and observational work suggests that the scattered images giving rise to scintillation arcs may be one-dimensional perpendicular to the line of sight to the pulsar (e.g. Trang & Rickett 2007; Briskin et al. 2010). Exploring a 1D scattered image model is desirable not only because it is motivated by previous work, but also because it simplifies the relationship between the brightness function and secondary spectrum. In the following section, we explore a 1D Gaussian scattered image in order to determine a mechanism for frequency-dependent scintillation arc widths. The arc width is taken to be the width in fringe frequency, as determined in Chapter 4 through cross-cuts of the secondary spectrum.

## 5.2 A 1D Scattered Image Model

Consider a 1D scattered image consisting of a Gaussian brightness function of the form

$$B(\theta) = B_0 e^{-(\theta/\theta_s)^2}, \quad (5.1)$$

where  $B_0$  is a constant,  $\theta$  is the angle at which the ray emerges from the screen (with the pulsar at the origin) and  $\theta_s$  is the scale size of the Gaussian image core. Cordes et al. (2006) show that for 1D images, the secondary spectrum can be written as a product of two brightness functions:

$$S_2(p, q) = \frac{1}{2|q|} B(\theta_+) B(\theta_-) \quad (5.2)$$

where the deflection angles are given by

$$\theta_+ = \frac{p - q^2}{2q} \quad (5.3)$$

$$\theta_- = \frac{p + q^2}{2q}. \quad (5.4)$$

The dimensionless variables  $p$  and  $q$  for delay and fringe frequency are as described in Section 2.2.2, expressed in terms of two deflection angles  $\theta_1$  and  $\theta_2$  and simplified to one dimension:

$$\begin{aligned} p &= \theta_2^2 - \theta_1^2 \\ &= (\theta_{2,x} + \theta_{1,x})(\theta_{2,x} - \theta_{1,x}) \\ q &= (\theta_2 - \theta_1) \cdot \mathbf{v}_{\text{eff}} \\ &= (\theta_{2,x} - \theta_{1,x})v_{\text{eff}}, \end{aligned}$$

where the deflection angles and  $\mathbf{v}_{\text{eff}}$  are taken to be aligned with the  $\theta_x$  direction. The deflection angle components are related as  $\theta_+ = \theta_{2,x}$  and  $\theta_- = \theta_{1,x}$ .

At constant delay  $p = p_0$ , the slope of the deflection angle  $\theta_+$  is given by

$$\frac{d\theta_+}{dq} = -\frac{p_0}{2q^2} - \frac{1}{2}. \quad (5.5)$$

Along a scintillation arc  $p_0 = q^2$  and  $\theta_+ = 0$ , in which case

$$\frac{d\theta_+}{dq} = -1. \quad (5.6)$$

A plot of  $\theta_+$  and  $\theta_-$  as a function of  $q$  for several values of constant delay  $p_0$  is shown in Fig. 5.2. At the point  $p_0 = q^2$ ,  $\theta_-(q)$  is approximately constant, and the profile of the secondary spectrum  $S_2(p, q)$  can be approximated as the profile of  $B(\theta_+)$ :

$$S_2(p, q) \sim \frac{1}{2|q|} B(\theta_+). \quad (5.7)$$

The angle  $\theta_+$  can be Taylor-expanded around the crossing point of the arc as

$$\begin{aligned} \theta_+ &\approx 0 + \frac{d\theta_+}{dq}(\Delta q) + \dots \\ &\approx -\Delta q \end{aligned} \quad (5.8)$$

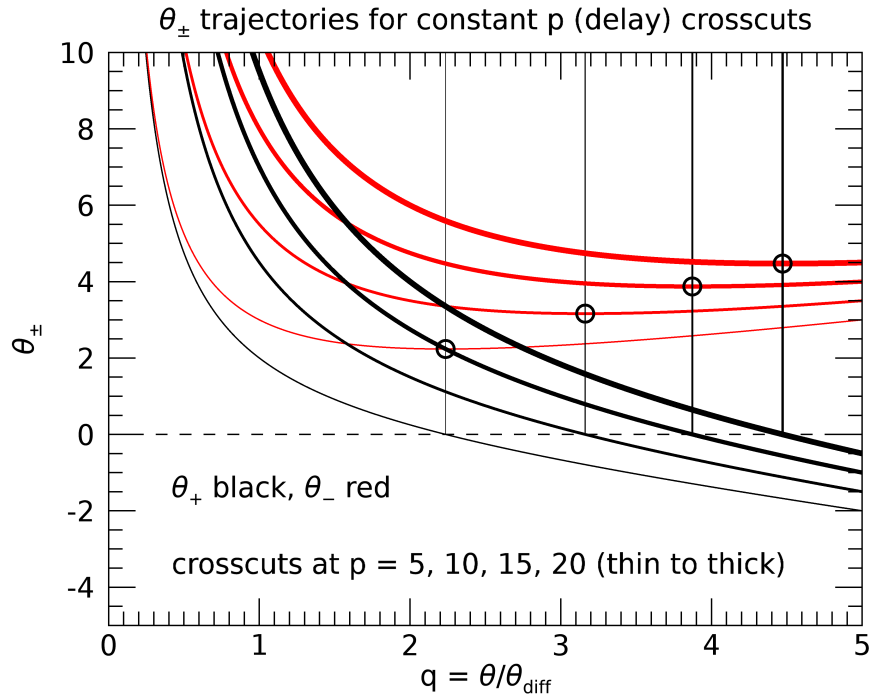


Figure 5.2: Behavior of the angles  $\theta_{+}$  (in black) and  $\theta_{-}$  (in red) as a function of dimensionless fringe frequency  $q$  for crosscuts of the secondary spectrum at dimensionless delays  $p = 5, 10, 15, 20$  (thin to thick lines). The secondary spectrum is assumed to arise from a 1D scattered image of the form given in Eq. 5.1. The circled points indicate the value of  $\theta_{-}$  when the corresponding  $\theta_{+} = 0$  as the crosscut passes across the center of the scintillation arc.

where  $\Delta q$  is the width in fringe frequency,  $(q - q_0)$ , and we have suppressed higher order terms. Thus the brightness function  $B(\theta_+)$  can be rewritten as

$$B(\theta_+) = B_0 e^{-(\Delta q/\theta_s)^2}. \quad (5.9)$$

If we ignore the factor of  $1/2|q|$  in  $S_2(p, q)$ , then at the point where  $B(\theta_+) = B_0/e$ , the fringe frequency width of the scintillation arc on one side of  $S_2(p, q)$  is  $\Delta q = \theta_s$ , and the full width ( $FW$ ) of the scintillation arc is

$$FW = 2\theta_s. \quad (5.10)$$

If we incorporate the factor of  $1/2|q|$  in  $S_2(p, q)$ , we have

$$S_2(p, q) \sim \frac{1}{2|q|} B(\theta_+) = \frac{1}{2|q|} B_0 e^{-(\Delta q/\theta_s)^2}. \quad (5.11)$$

A numerical analysis reveals that when  $\theta_s \ll q_0$  and  $p_0$  is large, the factor of  $1/2|q|$  has negligible effect on  $S_2(p, q)$ , and the width of the arc is well approximated by  $2\theta_s$ .

The above analysis does not incorporate an angle  $\psi$  between the scattered image and the effective velocity. Assuming such an angle, the deflection angles take the form  $\theta^2 = \theta_x^2 + \theta_y^2$ , where  $\theta_y = \theta_x \tan \psi$ . Given that  $\mathbf{v}_{\text{eff}}$  is still aligned with the  $\theta_x$  direction, the dimensionless delay and fringe frequency become

$$\begin{aligned} p &= (\theta_{2,x})^2 + (\theta_{2,y})^2 - (\theta_{1,x})^2 - (\theta_{1,y})^2 \\ &= (\theta_{2,x})^2 (1 + \tan^2 \psi) - (\theta_{1,x})^2 (1 + \tan^2 \psi) \\ &= (\theta_{2,x} + \theta_{1,x})(\theta_{2,x} - \theta_{1,x}) \sec^2 \psi \\ q &= (\theta_{2,x} - \theta_{1,x}) v_{\text{eff}}. \end{aligned}$$

The deflection angles  $\theta_+$  and  $\theta_-$  become

$$\begin{aligned} \theta_+ &= \frac{p}{2q \sec^2 \psi} - \frac{q}{2} \\ \theta_- &= \frac{p}{2q \sec^2 \psi} + \frac{q}{2}. \end{aligned}$$

At the point  $\theta_+ = 0$ ,  $p_0 = q^2 \sec^2 \psi$  and

$$\frac{d\theta_+}{dq} = -1$$

implying that incorporating  $\psi$  does not change the relationship between  $\Delta q$  and  $\theta_s$ .

It thus follows that for a Gaussian 1D scattered image, there is a simple mapping from the brightness function to the scintillation arc width. A frequency-dependent arc width can be accounted for by a frequency dependent-angle

$$\theta_s = \theta_{s,\text{ref}} \left( \frac{\nu}{\nu_{\text{ref}}} \right)^n \quad (5.12)$$

where  $\theta_{s,\text{ref}}$  and  $\nu_{\text{ref}}$  are the reference scattering angle and observing frequency and  $n$  is some constant. In this case, the scintillation arc broadens as a consequence of the inherent frequency dependent behavior of the scattered image.

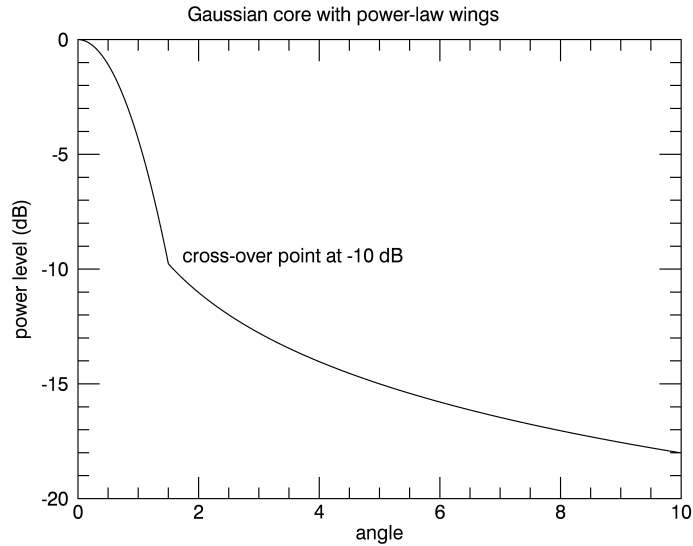


Figure 5.3: The brightness function for a scattered image consisting of a Gaussian core with an amplitude  $B_0 = 1$  and a width  $\theta_1 = 1$ , which crosses over at a power level of -10 dB to a power-law with an index of 2.

### 5.3 A 1D Gaussian/Power-Law Model

Consider a 1D scattered image that has a Gaussian core of the same form as Eq. 5.1 with  $B_0 = 1$  and a width  $\theta_s = 0.1$ , which crosses over at a power level of -20 dB to a power-law with an index of 2. The brightness function for a similar scattered image (but with a cross over point of -10 dB) is shown in Fig. 5.3. The secondary spectra calculated from this brightness distribution for  $\psi = 0^\circ, 20^\circ, 40^\circ$ , and  $60^\circ$  are shown in Fig. 5.4 through Fig. 5.7. As  $\psi$  increases, the arc spans a narrower range of  $q$ .

#### 5.3.1 A 1D Mechanism for Broadening Arcs

Cross-cuts of secondary spectra for  $\psi = 0^\circ$  and Gaussian widths ranging from  $\theta_s = 0.1$  to  $\theta_s = 0.6$ , taken at constant delay values  $p = 5, 10, 15$ , and  $20$ , are shown in Fig. 5.8 through Fig. 5.11. The only parameter changing between each figure is the width of the Gaussian core. The broadening of the cross-cut intensity affirms the direct connection between an increase in the width of the brightness function's core and an increase in the scintillation arc width, as analytically found in Section 5.2. Moreover, this increase in arc width appears equal for cross-cuts taken at different delay values.

Cross-cuts of secondary spectra at delay  $p = 10$  for values of  $\psi$  ranging from  $0^\circ$  to  $80^\circ$  are shown in Fig. 5.12. As  $\psi$  increases, the peak in cross-cut intensity moves to lower  $q$ , as indicated in the secondary spectra when the arc moves to lower ranges of  $q$  for higher values of  $\psi$  (see Fig. 5.4-Fig. 5.7). The cross-cut intensity also qualitatively follows the same behavior as the original brightness function. In logarithmic intensity, the cross-cut appears parabolic, corresponding to a Gaussian distribution in linear intensity, and sharply cuts off to power-law "wings." This qualitative correspondence between cross-cuts of the secondary spectrum and the original brightness function suggests that cross-cuts of scintillation arcs are direct indications of the form of the original scattered image.

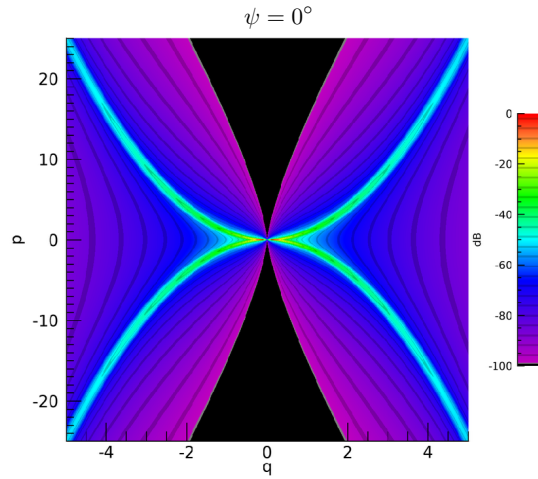


Figure 5.4: Secondary spectrum extracted from a 1D scattered image consisting of a Gaussian core with  $B_0 = 1$  and  $\theta_s = 0.1$ , which crosses over at a power level of -20 dB to a power-law with an index of 2. Here the angle between the scattered image and the effective velocity is  $\psi = 0^\circ$ .

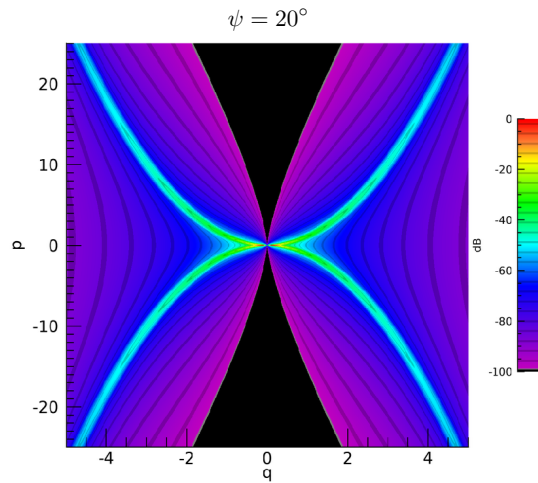


Figure 5.5: Secondary spectrum extracted from the 1D Gaussian/power-law image of the same parameters as in Fig. 5.4, but here  $\psi = 20^\circ$ .

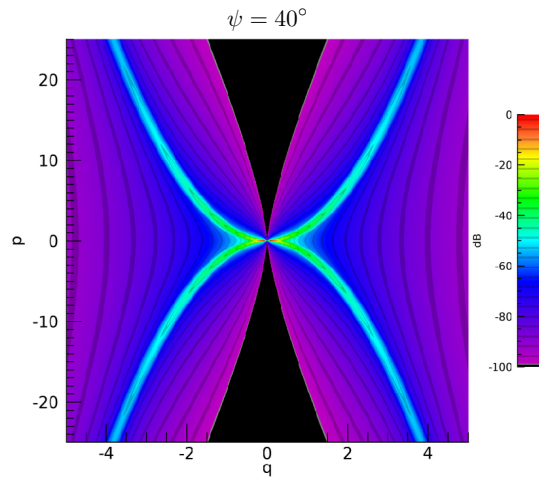


Figure 5.6: Secondary spectrum extracted from the 1D Gaussian/power-law image of the same parameters as in Fig. 5.4, but here  $\psi = 40^\circ$ .

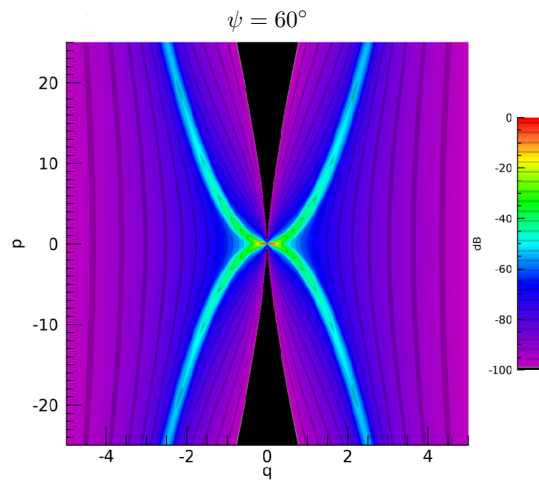


Figure 5.7: Secondary spectrum extracted from the 1D Gaussian/power-law image of the same parameters as in Fig. 5.4, but here  $\psi = 60^\circ$ .

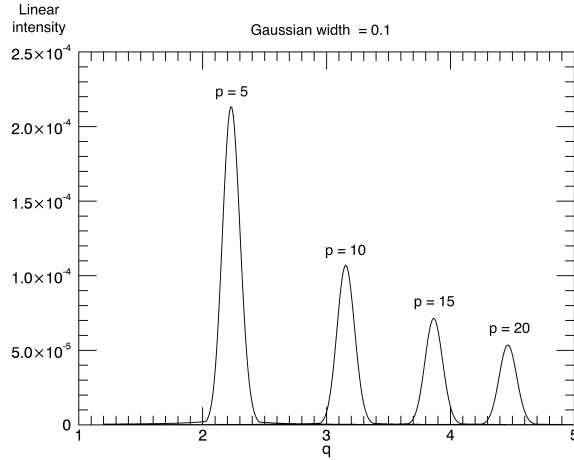


Figure 5.8: Cross-cuts of the linear intensity as a function of  $q$  at  $p = 5, 10, 15,$  and  $20$ . The scattered image was taken to have a Gaussian core width of 0.1, angled at  $\psi = 0^\circ$  with respect to the effective velocity.

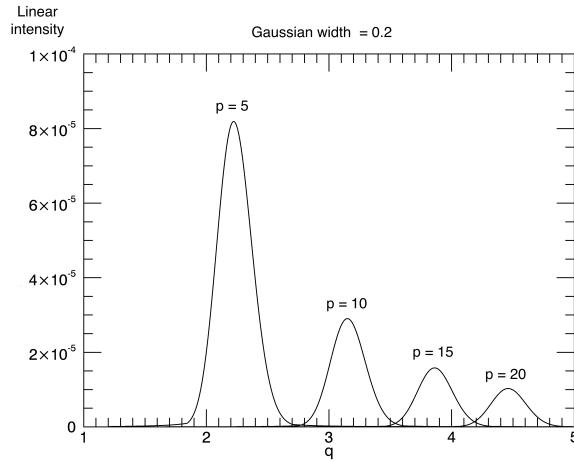


Figure 5.9: Cross-cuts of the linear intensity as a function of  $q$  at  $p = 5, 10, 15,$  and  $20$ . The scattered image was taken to have a Gaussian core width of 0.2, angled at  $\psi = 0^\circ$  with respect to the effective velocity.

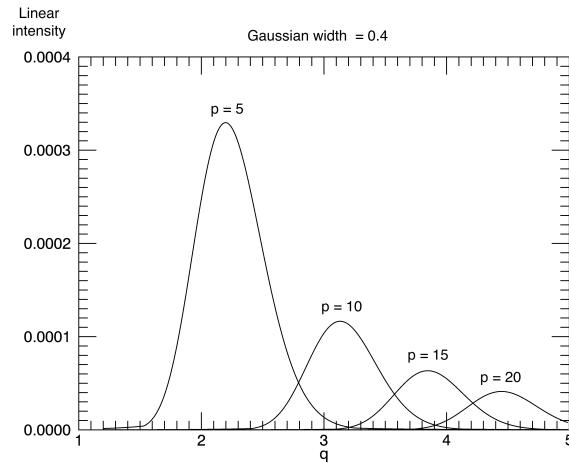


Figure 5.10: Cross-cuts of the linear intensity as a function of  $q$  at  $p = 5, 10, 15,$  and  $20$ . The scattered image was taken to have a Gaussian core width of  $0.4$ , angled at  $\psi = 0^\circ$  with respect to the effective velocity.

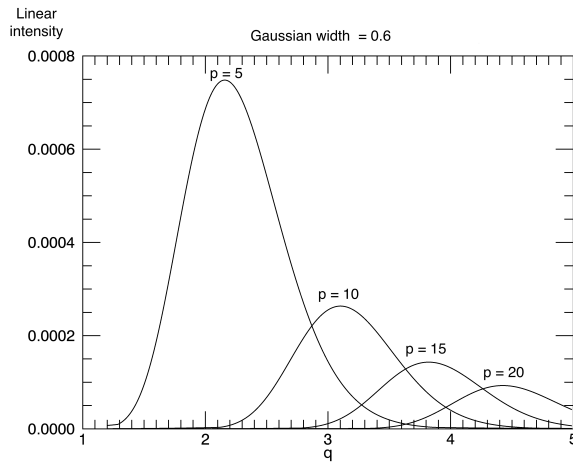


Figure 5.11: Cross-cuts of the linear intensity as a function of  $q$  at  $p = 5, 10, 15,$  and  $20$ . The scattered image was taken to have a Gaussian core width of  $0.6$ , angled at  $\psi = 0^\circ$  with respect to the effective velocity.

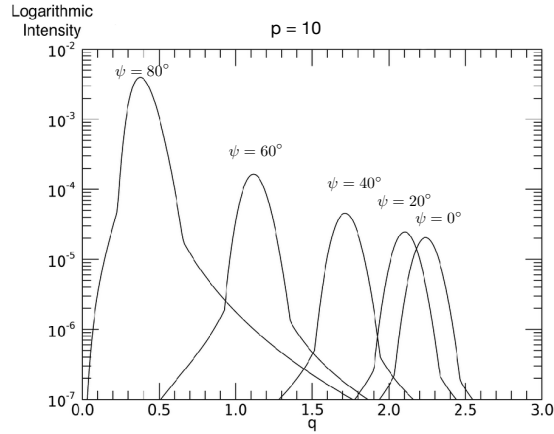


Figure 5.12: Cross-sections of secondary spectra at  $p = 10$  for values of  $\psi$  ranging from  $0^\circ$  to  $80^\circ$ . All other parameters of the scattered image were kept the same.

## 5.4 A 1D Model of B1133+16

A 1D model of the scattered image for B1133+16 has already been found appropriate by Barney Rickett (UC San Diego). Fitting a 1D brightness function of the form in Eq. 5.2 to secondary spectra of B1133+16 taken at 1450, 432, and 327 MHz, Rickett finds that the width of the core of the brightness function scales with frequency as  $\nu^{-1.7 \pm 0.7}$ , which agrees with our empirical result that the fringe frequency width of scintillation arcs observed in B1133+16 follow a frequency scaling of  $\nu^{-1.8 \pm 0.1}$  (Chapter 4). This frequency scaling is also close to the expected frequency dependence of the scattering angle in a plasma,  $\nu^{-2}$ . A 1D, frequency dependent brightness function appears to be a good model for B1133+16 (Rickett 2018).

## 5.5 Discussion

One-dimensional modeling is attractive for several reasons. Not only is the relationship between the pulsar scattered image and secondary spectrum very simple, but it also leads to a direct relationship between the

image brightness function and the fringe frequency width of a scintillation arc. In the case of a Gaussian brightness function, the (dimensionless) fringe frequency width of the arc is equal to twice the Gaussian width ( $\Delta q = 2\theta_s$ ). In this 1D scenario the frequency dependence of scintillation arc widths thus naturally falls out of a frequency-dependent brightness function. Our qualitative examination of the 1D Gaussian/power-law model confirms that a broadening of the Gaussian core gives rise to thicker arcs in the secondary spectrum. Furthermore, the scintillation arc cross-cuts in the Gaussian/power-law model suggest that the shape of a cross-cut is directly related to the shape of the original brightness function, raising the possibility that arc cross-cuts might be used to model the pulsar scattered image.

In the case of B1133+16, a 1D brightness function seems an appropriate model of the pulsar's scattered image. The close correspondence between Rickett's arc width frequency dependence, based on a 1D brightness function, and our result from scintillation arc cross-cuts, affirms the utility of arc width frequency dependence as a predictive test for models.

## Chapter 6

# Conclusions

Determining the physical origin of scintillation arcs has important consequences for interstellar medium studies and the detection of gravitational waves with pulsars. While numerous models for the production of scintillation arcs have been proposed, few have produced predictions that are easily comparable with observation. This thesis demonstrates how the frequency-dependent behavior of scintillation arcs can be used as a predictive test for models.

B1133+16 is a particularly useful pulsar for testing the production of scintillation arcs. Studied for decades, its well-known, simple behavior at multiple frequencies makes it an ideal test case for modeling. Measurements of its fringe frequency arc widths at four frequencies suggest that for B1133+16, the angular width of the pulsar image scales as  $\nu^{-1.8 \pm 0.1}$ . Moreover, this width scaling agrees with a 1D brightness function, suggesting that the scattered image for B1133+16 is one-dimensional perpendicular to the line of sight. Our exploration of a 1D mechanism for broadening arc widths suggests that the arc width frequency dependence observed in B1133+16 arises directly from the core of the brightness function broadening at lower frequencies.

One-dimensional models of pulsar scattered images appear particularly useful, not only because they are straightforward to construct, but also because they lead to a simple relationship between the image brightness

function and the scintillation arc width, making them easy to compare to observation. In addition to demonstrating how a model of a 1D brightness function can be used to make predictions about the frequency dependent behavior of scintillation arc widths, we have shown that crosscuts of scintillation arcs might be directly related to the brightness function underlying the secondary spectrum. This result suggests that to understand the nature of the scattered image, one may only need to look at the shape of a scintillation arc cross-cut.

This thesis has also demonstrated how annual curvature modulation may be used to determine the scattering screen location and orientation. While B1133+16 has too high a transverse velocity to narrowly constrain the screen location  $s$  and orientation  $\psi$ , the results show that a somewhat constrained range of  $s$  and  $\psi$  are possible. Two of the scattering screens may be as close to each other as 35 parsecs (a distance of  $s = 0.1$ ). If an independent measure of  $s$  is made, for example by Very Long Baseline Interferometry (VLBI), then  $\psi$  could be constrained with the annual modulation model for B1133+16. However, it is likely easier to detect annual curvature modulation in slower pulsars.

Overall, our examination of B1133+16 suggests the following main constraints for modeling efforts making use of this pulsar:

- The screen locations and orientations are in the range  $0.15 < s < 0.84$  and  $0^\circ < \psi < 80^\circ$ .
- The fringe frequency width of the scintillation arcs scales with observing frequency according to  $\Delta f_t \propto \nu^{-0.8 \pm 0.1}$ .
- The scintillation arc widths are constant over delay.
- The intensity of the scintillation arc as a function of fringe frequency is well-approximated by a Gaussian distribution.

It would be useful to extend a multi-frequency analysis to more pulsars. Do other pulsars exhibit the same arc width frequency dependence? Such consistency would point to a ubiquitous physical origin for scintillation arcs. Our analysis of B1133+16 only took advantage of data taken in 2015, but

there are 20 years of data on this pulsar that could be included. Studying a longer time span of data would be particularly useful for determining whether the asymmetry observed in the scintillation arc widths arises from power “traveling” along the arcs, as was first seen by Hill et al. (2005). A longer data set, coupled with a more precise method of measuring arc curvatures, would also better constrain the annual modulation model for B1133+16.

We plan to further explore the potential of 1D models for the production of scintillation arcs. The simple relationship between a 1D brightness function and scintillation arc width demonstrates the utility of arc width frequency dependence as a predictive test. Measurements of scintillation arc widths provide a crucial quantitative step in connecting a pulsar scattered image, brightness function, and the resultant secondary spectrum.

## Appendix A

# Derivation of Annual Curvature Modulation

Following the Tuntsov formalism (Tuntsov 2017), we consider a linear scattering image, for which an incident ray is scattered in a direction

$$\boldsymbol{\theta} = \boldsymbol{\theta}_0 + \hat{\rho}t, \quad (\text{A.1})$$

where  $\hat{\rho}$  gives the direction of the linear scattering image, and  $t$  lies in the domain of all positions along the line  $\boldsymbol{\theta}$  where images form. Recall that the curvature  $\eta$  is given by:

$$\eta = \frac{D\lambda^2}{2c} \frac{s(1-s)}{\hat{\rho}\mathbf{v}_{\text{eff}}^2} \quad (\text{A.2})$$

where  $D$  is the distance to the pulsar,  $s$  is the screen location, and  $\mathbf{v}_{\text{eff}}$  is given by:

$$\mathbf{v}_{\text{eff}} = (1-s)\mathbf{v}_{\text{p}\perp} + s\mathbf{v}_{\text{obs}\perp} - \mathbf{v}_{\text{scr}\perp}. \quad (\text{A.3})$$

As stated in Chapter 3, observer velocity changes with Earth's orbit according to an ellipse:

$$\mathbf{v}_{\text{obs}\perp} = \mathbf{v}_{\odot} + \hat{e}_1 v_1 \cos \phi + \hat{e}_2 v_2 \sin \phi \quad (\text{A.4})$$

where  $\mathbf{v}_{\odot}$  is the velocity of the Solar System barycentre (roughly the velocity of the Sun),  $\hat{e}_1, \hat{e}_2, v_1, v_2$  are the directions and magnitudes of the major and

minor axes of the ellipse ( $\hat{e}_1 v_1 \cdot \hat{e}_2 v_2 = 0$ ), and  $\phi$  is the eccentric anomaly, which defines the angular position of Earth on the ellipse.

Since  $\mathbf{v}_\odot$  is constant, plugging Eq. A.4 into Eq. A.3 yields

$$\begin{aligned}\mathbf{v}_{\text{eff}} &= (1-s)\mathbf{v}_{\text{p}\perp} + s[\hat{e}_1 v_1 \cos \phi + \hat{e}_2 v_2 \sin \phi] - \mathbf{v}_{\text{scr}\perp} \\ &= ((1-s)\mathbf{v}_{\text{p}\perp} - \mathbf{v}_{\text{scr}\perp}) + s[\hat{e}_1 v_1 \cos \phi + \hat{e}_2 v_2 \sin \phi].\end{aligned}$$

Squaring  $\mathbf{v}_{\text{eff}}$ , we have

$$\mathbf{v}_{\text{eff}}^2 = \left(\frac{v_{SL}^\rho}{\hat{\rho}}\right)^2 + \frac{2}{\hat{\rho}}v_{SL}^\rho s[\hat{e}_1 v_1 \cos \phi + \hat{e}_2 v_2 \sin \phi] + s^2[\hat{e}_1 v_1 \cos \phi + \hat{e}_2 v_2 \sin \phi]^2 \quad (\text{A.5})$$

where

$$v_{SL}^\rho \equiv \hat{\rho}(s\mathbf{v}_{\text{p}\perp} - \mathbf{v}_{\text{scr}\perp}).$$

The last term in Eq. A.5 can be expanded:

$$\begin{aligned}[\hat{e}_1 v_1 \cos \phi + \hat{e}_2 v_2 \sin \phi]^2 &= v_1^2 \cos^2 \phi + 2\hat{e}_1 v_1 \cdot \hat{e}_2 v_2 \sin \phi \cos \phi + v_2^2 \sin^2 \phi \\ &= v_1^2 \cos^2 \phi + v_2^2 \sin^2 \phi + \hat{e}_1 v_1 \cdot \hat{e}_2 v_2 [\sin 2\phi + \sin 0] \\ &= v_1^2 \cos^2 \phi + v_2^2 \sin^2 \phi + \hat{e}_1 v_1 \cdot \hat{e}_2 v_2 \sin 2\phi \\ &= \frac{1}{2}[(v_1^2 + v_2^2) + (v_1^2 \cos 2\phi - v_2^2 \cos 2\phi)].\end{aligned}$$

Solving for inverse curvature, we have

$$\begin{aligned}\frac{\lambda^2 D}{2c\eta} &= \frac{(v_{SL}^\rho)^2}{s(1-s)} + \frac{2\hat{\rho}(v_{SL}^\rho)}{(1-s)}v_1 \cos \phi + \frac{2\hat{\rho}(v_{SL}^\rho)}{(1-s)}v_2 \sin \phi \\ &\quad + \frac{s}{2(1-s)}(v_1^2 + v_2^2) + \frac{s}{2(1-s)}(v_1^2 - v_2^2) \cos 2\phi \quad (\text{A.6})\end{aligned}$$

# Bibliography

- Armstrong, J. W., Rickett, B. J., & Spangler, S. R. 1995, *ApJ*, 443, 209
- Bhat, N. D. R., Ord, S. M., Tremblay, S. E., McSweeney, S. J., & Tingay, S. J. 2016, *ApJ*, 818, 86
- Breitschwerdt, D., de Avillez, M. A., Feige, J., & Dettbarn, C. 2012, *Astronomische Nachrichten*, 333, 486
- Brisken, W. 2009, in *New Science Enabled by Microarcsecond Astrometry*, held 21-23 July 2009 in Socorro, NM., 21
- Brisken, W. F., Macquart, J.-P., Gao, J. J., et al. 2010, *ApJ*, 708, 232
- Burke-Spolaor, S. 2015, ArXiv e-prints, arXiv:1511.07869
- Caballero, I., & Wilms, J. 2012, *Mem. Societa Astronomica Italiana*, 83, 230
- Cordes, J. M., & Lazio, T. J. W. 2002, ArXiv Astrophysics e-prints, astro-ph/0207156
- Cordes, J. M., & Rickett, B. J. 1998, *ApJ*, 507, 846
- Cordes, J. M., Rickett, B. J., Stinebring, D. R., & Coles, W. A. 2006, *ApJ*, 637, 346
- Czesla, S. 2017, `baryCorr()`: calculate barycentric correction, PyAstronomy, [hs.uni-hamburg.de](http://hs.uni-hamburg.de)
- D'Alessandro, F. 1996, *APSS*, 246, 73

## BIBLIOGRAPHY

---

- Grenier, I. A., & Harding, A. K. 2015, *Comptes Rendus Physique*, 16, 641
- Gurnett, D. A., Kurth, W. S., Burlaga, L. F., & Ness, N. F. 2013, *Science*, 341, 1489
- Haverkorn, M., & Spangler, S. R. 2013, *Space Science Reviews*, 178, 483
- Herbst, E., & van Dishoeck, E. F. 2009, *Annual Review of Astron and Astrophys*, 47, 427
- Hill, A. S., Stinebring, D. R., Asplund, C. T., et al. 2005, *ApJL*, 619, L171
- Hill, A. S., Stinebring, D. R., Barnor, H. A., Berwick, D. E., & Webber, A. B. 2003, *ApJ*, 599, 457
- Hobbs, G., Lorimer, D. R., Lyne, A. G., & Kramer, M. 2005, *MNRAS*, 360, 974
- Kalopotharakos, C., Kazanas, D., Harding, A., & Contopoulos, I. 2012, *ApJ*, 749, 2
- Kargaltsev, O., Cerutti, B., Lyubarsky, Y., & Striani, E. 2015, *Space Science Reviews*, 191, 391
- Kaspi, V. M., & Kramer, M. 2016, *ArXiv e-prints*, arXiv:1602.07738
- Kirsten, F., Vlemmings, W., Campbell, R. M., Kramer, M., & Chatterjee, S. 2015, *Astronomy and Astrophysics*, 577, A111
- Kramer, M. 2004, in *Lecture Notes in Physics*, Berlin Springer Verlag, Vol. 648, *Astrophysics, Clocks and Fundamental Constants*, ed. S. G. Karshenboim & E. Peik, 33–54
- Kramer, M., & Stairs, I. H. 2008, *Annual Review of Astron and Astrophys*, 46, 541
- Lam, M. T., Cordes, J. M., Chatterjee, S., et al. 2017, *ApJ*, 834, 35
- Lommen, A. N., & Demorest, P. 2013, *Classical and Quantum Gravity*, 30, 224001

## BIBLIOGRAPHY

---

- Lorimer, D. R. 2008, *Living Reviews in Relativity*, 11, arXiv:0811.0762
- Lyne, A. 1999, in *Pulsar Timing, General Relativity and the Internal Structure of Neutron Stars*, ed. Z. Arzoumanian, F. Van der Hooft, & E. P. J. van den Heuvel, 141
- Lyne, A., & Graham-Smith, F. 2012, *Pulsar Astronomy* (Cambridge University Press)
- Lyne, A. G., Manchester, R. N., & Taylor, J. H. 1985, *MNRAS*, 213, 613
- Manchester, R. N., Hobbs, G. B., Teoh, A., & Hobbs, M. 2005, *VizieR Online Data Catalog*, 7245
- Marshall, D. J., Robin, A. C., Reylé, C., Schultheis, M., & Picaud, S. 2006, *Astronomy and Astrophysics*, 453, 635
- McKee, C. F., & Ostriker, J. P. 1977, *ApJ*, 218, 148
- McSweeney, S. 2017, *parabfit: fits a parabola to a secondary spectrum of the pulsar*, Private Communication
- Pen, U.-L., & King, L. 2012, *MNRAS*, 421, L132
- Pen, U.-L., & Levin, Y. 2014, *MNRAS*, 442, 3338
- Popping, G., Somerville, R. S., & Galametz, M. 2017, *MNRAS*, 471, 3152
- Putney, M. L., & Stinebring, D. R. 2006, *Chinese Journal of Astronomy and Astrophysics Supplement*, 6, 233
- Rickett, B. 2018, Private Communication
- Rickett, B., Stinebring, D., Coles, B., & Jian-Jian, G. 2011, in *American Institute of Physics Conference Series*, Vol. 1357, American Institute of Physics Conference Series, ed. M. Burgay, N. D'Amico, P. Esposito, A. Pellizzoni, & A. Possenti, 97–100
- Rickett, B. J. 1990, *Annual Review of Astron and Astrophys*, 28, 561

BIBLIOGRAPHY

---

- Rickett, B. J. 2007, in *Astronomical Society of the Pacific Conference Series*, Vol. 365, *SINS - Small Ionized and Neutral Structures in the Diffuse Interstellar Medium*, ed. M. Haverkorn & W. M. Goss, 207
- Rudnitskii, A. G., Popov, M. V., & Soglasnov, V. A. 2017, *Astronomy Reports*, 61, 393
- Savage, B. D., & Mathis, J. S. 1979, *Annual Review of Astron and Astrophys*, 17, 73
- Sesana, A. 2013, *Classical and Quantum Gravity*, 30, 224014
- Stinebring, D. 2007, in *Astronomical Society of the Pacific Conference Series*, Vol. 365, *SINS - Small Ionized and Neutral Structures in the Diffuse Interstellar Medium*, ed. M. Haverkorn & W. M. Goss, 254
- Stinebring, D. R., Hill, A. S., McLaughlin, M. A., et al. 2003, in *Astronomical Society of the Pacific Conference Series*, Vol. 302, *Radio Pulsars*, ed. M. Bailes, D. J. Nice, & S. E. Thorsett, 263
- Stinebring, D. R., Hill, A. S., & Ransom, S. M. 2005, in *Astronomical Society of the Pacific Conference Series*, Vol. 328, *Binary Radio Pulsars*, ed. F. A. Rasio & I. H. Stairs, 349
- Stinebring, D. R., McLaughlin, M. A., Cordes, J. M., et al. 2001, *ApJL*, 549, L97
- Trang, F. S., & Rickett, B. J. 2007, *ApJ*, 661, 1064
- Tuntsov, A. 2017, Private Communication
- Usov, V. V. 2003, in *American Institute of Physics Conference Series*, Vol. 669, *Plasma Physics*, ed. I. S. Falconer, R. L. Dewar, & J. Khachan, 766–768
- Walker, M. A., Tuntsov, A. V., Bignall, H., et al. 2017, *ApJ*, 843, 15
- Wilson, T. L., & Rood, R. 1994, *Annual Review of Astron and Astrophys*, 32, 191

BIBLIOGRAPHY

---

Yao, J. M., Manchester, R. N., & Wang, N. 2017, ApJ, 835, 29

I affirm I adhered to the Honor Code on this assignment.